



HAL
open science

Size distribution and optical properties of African mineral dust after intercontinental transport

Cyrielle Denjean, Paola Formenti, Karine Desboeufs, Servanne Chevaillier, Sylvain Triquet, Michel Maillé, Mathieu Cazaunau, Benoit Laurent, Olga L. Mayol-Bracero, Pamela Vallejo, et al.

► To cite this version:

Cyrielle Denjean, Paola Formenti, Karine Desboeufs, Servanne Chevaillier, Sylvain Triquet, et al.. Size distribution and optical properties of African mineral dust after intercontinental transport. *Journal of Geophysical Research: Atmospheres*, 2016, 121, pp.7117-7138. 10.1002/2016JD024783. insu-03737484

HAL Id: insu-03737484

<https://insu.hal.science/insu-03737484>

Submitted on 25 Jul 2022

HAL is a multi-disciplinary open access archive for the deposit and dissemination of scientific research documents, whether they are published or not. The documents may come from teaching and research institutions in France or abroad, or from public or private research centers.

L'archive ouverte pluridisciplinaire **HAL**, est destinée au dépôt et à la diffusion de documents scientifiques de niveau recherche, publiés ou non, émanant des établissements d'enseignement et de recherche français ou étrangers, des laboratoires publics ou privés.

Copyright

RESEARCH ARTICLE

10.1002/2016JD024783

Key Points:

- Microphysical and optical properties of mineral dust independent of origin after transport
- Size distribution of mineral dust after long-range transport may resemble to short range
- Visible mass extinction efficiency and single-scattering albedo around 1.1–1.5 m² g⁻¹ and 0.97–0.98

Correspondence to:

P. Formenti,
paola.formenti@lisa.u-pec.fr

Citation:

Denjean, C., et al. (2016), Size distribution and optical properties of African mineral dust after intercontinental transport, *J. Geophys. Res. Atmos.*, 121, 7117–7138, doi:10.1002/2016JD024783.

Received 10 JAN 2016

Accepted 12 MAY 2016

Accepted article online 22 MAY 2016

Published online 23 JUN 2016

Size distribution and optical properties of African mineral dust after intercontinental transport

Cyrielle Denjean^{1,2}, Paola Formenti¹, Karine Desboeufs¹, Servanne Chevaillier¹, Sylvain Triquet¹, Michel Maillé¹, Mathieu Cazaunau¹, Benoit Laurent¹, Olga L. Mayol-Bracero³, Pamela Vallejo³, Mariana Quiñones³, Ian E. Gutierrez-Molina³, Federico Cassola⁴, Paolo Prati⁴, Elisabeth Andrews⁵, and John Ogren⁵

¹LISA, UMR CNRS 7583, Université Paris Est Créteil et Université Paris Diderot, Institut Pierre Simon Laplace, Créteil, France, ²Now at Centre National de Recherches Météorologiques, MétéoFrance, Toulouse, France, ³Department of Environmental Science, University of Puerto Rico, San Juan, Puerto Rico, USA, ⁴Department of Physics and INFN, University of Genoa, Genoa, Italy, ⁵NOAA/ESRL Global Monitoring Division, Boulder, Colorado, USA

Abstract The transatlantic transport of mineral dust from Africa is a persistent atmospheric phenomenon, clue for understanding the impacts of dust at the global scale. As part of the DUST Aging and Transport from Africa to the Caribbean (Dust-ATTACK) intensive field campaign, the size distribution and optical properties of mineral dust were measured in June–July 2012 on the east coast of Puerto Rico, more than 5000 km from the west coast of Africa. During the recorded dust events, the PM₁₀ (particulate matter 10 micrometers or less in diameter) concentrations increased from 20 to 70 μg m⁻³. Remote sensing observations and modeling analysis were used to identify the main source regions, which were found in the Western Sahara, Mauritania, Algeria, Niger, and Mali. The microphysical and optical properties of the dust plumes were almost independent of origin. The size distribution of mineral dust after long-range transport may have modal diameters similar to those on the eastern side of the Atlantic short time after emission, possibly depending on height of transport. Additional submicron particles of anthropogenic absorbing aerosols (likely from regional marine traffic activities) can be mixed within the dust plumes, without affecting in a significant way the PM₁₀ absorption properties of dust observed in Puerto Rico. The Dust-ATTACK experimental data set may be useful for modeling the direct radiative effect of dust. For accurate representation of dust optical properties over the Atlantic remote marine region, we recommend mass extinction efficiency (MEE) and single-scattering albedo values in the range 1.1–1.5 m² g⁻¹ and 0.97–0.98, respectively, for visible wavelengths.

1. Introduction

The most recent model estimates indicate that, at the global scale, the aeolian emission of mineral dust from arid and semiarid areas ranges between 1000 and 3000 Tg yr⁻¹ [Ginoux et al., 2012] and represents about half of the mass of annual particle emission at the global scale [Boucher et al., 2013]. The largest fraction of these emissions comes from arid and semiarid areas in the African Sahara and Sahel, where satellite sensors consistently indicate the most widespread, persistent, and dense dust plumes found on Earth [Ben-Ami et al., 2009; Kim et al., 2014].

Once in the atmosphere, mineral dust plumes influence the global and regional climate, including the sea surface temperature [Yue et al., 2011], the development of tropical cyclones [Dunion and Velden, 2004], and precipitation [Creamean et al., 2013]. The processes involved are many. Dust interacts with radiation both by scattering and absorbing light in the shortwave and longwave spectral regions [Colarco et al., 2014] and may serve as cloud and ice condensation nuclei [DeMott et al., 2003; van den Heever et al., 2006]. In addition, dust can change the atmospheric composition through heterogeneous reactions with trace atmospheric organic and inorganic gases [Bauer et al., 2004; de Reus et al., 2005; Usher et al., 2003; Ndour et al., 2008]. Dust deposition can also have important implications for the global carbon cycle via the fertilization of the marine and terrestrial ecosystems [Duce et al., 1991; Jickells and Spokes, 2001]. Finally, mineral dust is a vector for bacteria and viruses and has thus a potential impact on human health [Kwon et al., 2002; Kellogg and Griffin, 2006; Perez et al., 2008], as well as on regional air quality via visibility impairment during strong events [Prospero, 1999].

Most of the remaining uncertainties in quantifying the impact of mineral dust on the Earth's climate are due to the disparities in the representation of the dust size distribution by models [Huneeus et al., 2011; Mahowald

et al., 2014]. Size distribution not only defines the emission and deposition fields for dust particles but also their lifetime and interactions with radiation, clouds, and water. *Huneus et al.* [2011] showed that, because of the differences in the representation of the particle size distribution, the dust mass extinction efficiency (MEE) ranged between 0.25 and $1.28 \text{ m}^2 \text{ g}^{-1}$ in the 15 models compared. The effect of this MEE range for a dust layer of given column concentration would translate into a fivefold difference in the column optical depth and hence a fivefold difference in the radiative forcing exerted at the top of the atmosphere (TOA). The *Huneus et al.* [2011] model comparison also revealed unexpected features such as a higher large-to-small particle ratio for transport in the Caribbean with respect to that of African dust at the source, possibly resulting from the growth of small particles by chemical reactions and/or by agglomeration during cloud processing. In contrast, measurements comparing the dust size distribution after inter-Atlantic transport showed a loss of coarse particles [*Formenti et al.*, 2001; *Maring et al.*, 2003a] and a notable reduction in TOA forcing [*Garrett et al.*, 2003].

The difficulties encountered by models in representing the dust size distribution mirror the challenge faced by measurements in representing the size range of those particles, which spans several order of magnitudes from $\sim 100 \text{ nm}$ to $\sim 100 \text{ }\mu\text{m}$ diameter [*Formenti et al.*, 2011; *Schladitz et al.*, 2009; *Weinzierl et al.*, 2009; *Ryder et al.*, 2013a]. Measuring the particle size distribution of mineral dust requires a multisensor approach combining techniques based on differing physical principles (aerodynamic settling, electrical mobility, and light scattering) and careful application of conversion algorithms [*Reid et al.*, 2003a; *Formenti et al.*, 2011].

The necessity of new sophisticated experimental data on the dust properties, and specifically on particle size, at the different times along their lifecycle, is a clear request of the modeling community [*Huneus et al.*, 2011; *Mahowald et al.*, 2014]. Various field campaigns in the last two decades have investigated the physicochemical and optical properties of mineral dust at emission and short-to-medium range transport distances over the African continent or just offshore. They are the African Monsoon Multidisciplinary Analysis [*Redelsperger et al.*, 2006] and its NASA component [*Chen et al.*, 2011], the Saharan Dust Experiment [*Haywood et al.*, 2003], the Bodelé Dust Experiment [*Todd et al.*, 2007], the Dust Outflow and Deposition to the Ocean [*McConnell et al.*, 2008], the Dust and Biomass Experiment [*Haywood et al.*, 2008], the Geostationary Earth Radiation Budget Intercomparison of Longwave and Shortwave radiation [*Haywood et al.*, 2011], the Saharan Mineral Dust Experiment 1 and 2 [*Heintzenberg*, 2009; *Ansmann et al.*, 2011], and FENNEC [*Washington et al.*, 2012]. Further from the emission source, the Puerto Rico Dust Experiment (PRIDE) [*Reid and Maring*, 2003] and the Puerto Rico African Dust and Cloud Study [*Raga et al.*, 2016; *Spiegel et al.*, 2014; *Valle-Díaz et al.*, 2016] investigated the impact of long-range transported mineral dust on the chemical and physical properties of aerosols, clouds, and rainwater in a tropical montane cloud forest. While significant progress has been made, the properties of mineral dust are still not well represented in models and further work is needed, particularly on dust size distribution and optical properties and their temporal evolution during long-range transport.

In this context, the Dust Aging and Transport from Africa to the Caribbean (Dust-ATTACK) project aimed at providing additional information on the aging of mineral dust following transport in the atmosphere. Dust-ATTACK was a ground-based field experiment conducted in the Cape San Juan Atmospheric Observatory in the Island of Puerto Rico in June–July 2012. Puerto Rico is an island territory of the United States located in the Caribbean Sea in the area bounded by $65.6\text{--}67.3 \text{ W}$ and $17.9\text{--}18.5 \text{ N}$. This paper discusses observations of the size distribution and optical properties of dust after long-range transport for a number of events and uses emission simulations and back trajectories to link the observations to source region and residence time in the atmosphere.

2. Methods

The main island of Puerto Rico is brick shaped and measures $180 \times 65 \text{ km}^2$. Much of its interior is a mountain range (Cordillera Central), with its spine running east-west along its length. The highest peak in this range, Cerro de Punta, is 1338 m above sea level.

The Dust-ATTACK field campaign took place between 20 June and 13 July 2012 at the low elevation Cape San Juan Puerto Rico Aerosol Observatory ($18^\circ 23' \text{ N}$, $65^\circ 37' \text{ W}$, 66 m above sea level) managed by the University of Puerto Rico. The station is a regional Global Atmosphere Watch (GAW) site and is a participant in both the National Oceanic and Atmospheric Administration–Earth System Research Laboratory (NOAA–ESRL, www.esrl.noaa.gov).



Figure 1. Location of the Cape San Juan (CPR) sampling station on the most northeastern tip of Puerto Rico.

noaa.gov/gmd/aero/net/cpr/index.html) collaborative aerosol network and the NASA AEROSOL ROBOTIC NETWORK (AERONET, <http://aeronet.gsfc.nasa.gov/>). The Observatory is known as CPR by GAW and in NOAA Earth System Research Laboratory's aerosol network and as Cape San Juan in NASA's AERONET. The site (Figure 1) is within the subtropical dry forest zone, has good exposure to the easterly trades (and hence African dust), and is free of major land masses upwind, minimizing the effects of anthropogenic aerosol sources.

2.1. Aerosol Measurements

In situ instrumentation providing observations of atmospheric aerosols is listed in Table 1. Most in situ aerosol instruments used the standard NOAA/ESRL/GMD aerosol inlet. This is a 10 m stack with the relative humidity of the sample air controlled as described in *Sheridan et al.* [2001]. This system allows transmission of particles of 10 μm in diameter with losses in number concentration within 10%, and within 5% for particles of diameters ranging between 0.01 and 1 μm. Aerosol measurements were made at relative humidity (RH) (<40%) conditions. The full description of protocols of operations is available at <ftp://ftp.wmo.int/Documents/PublicWeb/arep/gaw/gaw153.pdf>.

Table 1. List of Instruments Used in Study

| Instrument/model # | Measurement | Operating Parameters |
|---|---|---|
| Scanning Mobility Particle Sizer TSI Inc. (X-ray classifier, model 3080; Differential Mobility Analyzer, model 3081; and Condensation Particle Counter, model 3772) | Size distribution, nominal size range: nominal 11.8–593.5 nm | Aerosol flow rate 0.4 L min ⁻¹ , sheath flow rate 4 L min ⁻¹ , 3 min averaging time |
| Optical Particle Counter (GRIMM Inc. model 1.109) | Number size distribution, nominal size range: 0.25–32 μm, 31 channels | Sampling flow rate 1.2 L min ⁻¹ , 5 min averaging time |
| Integrating spectral nephelometer (TSI Inc. model 3563) | Scattering and backscattering coefficients at 450, 550, and 700 nm | Sampling flow rate 30 L min ⁻¹ , 1 min averaging time |
| Continuous Light Absorption Photometer (CLAP) NOAA/ESRL/GMD prototype | Absorption coefficient at 428, 528, and 652 nm | Sampling flow rate 1 L min ⁻¹ , 1 min averaging time |
| Tapered Element Oscillating Microbalance (TEOM) Thermo Fisher Scientific, model 1405-F | Mass concentration in the PM ₁₀ fraction | Sampling flow rate 1 L min ⁻¹ , 1 h running average of 6 min acquisition time |
| Picarro, model 3202 | CO and CO ₂ mixing ratio | Sampling flow rate 1 L min ⁻¹ , 5 min averaging time |
| UV photometric analyzer (Environmental SA, model O342M) | O ₃ mixing ratio | Sampling flow rate 1 L min ⁻¹ , 10 min averaging time |
| UV chemiluminescence analyzer (Environmental SA, model AC32M) | NO/NO ₂ /NO _x mixing ratio | Sampling flow rate 1 L min ⁻¹ , 10 min averaging time |
| Weather station Davis model 6160C, Vantage Pro | Wind direction, wind speed, air temperature, and relative humidity | 15 min averaging time |

The particle number size distribution was measured by a combination of a Scanning Mobility Particle Sizer (SMPS, TSI Inc.) and an optical particle counter (GRIMM Inc., model 1.109). The SMPS consisted of an electrostatic classifier (model 3080), a Differential Mobility Analyzer (model 3081) and a Condensation Particle Counter (CPC, model 3772). At the operating flow rates (sheath flow equal to 4 L min^{-1} and aerosol flow equal to 0.4 L min^{-1}), the SMPS sized particles of mobility diameter (D_{pm}) in the range 11.8–593.5 nm on a 2 min time period. A new measurement scan was started every 3 min. The GRIMM optical particle counter (OPC) measured the number concentration of particles of equivalent optical diameter (D_{po}) in the 0.25–32 μm range over 31 size channels. Particle sizing is based on the detection of light scattering between 46° and 133° at the working wavelength of the laser diode source (655 nm). The instrument was operated continuously at 5 min time resolution.

The particle volume scattering coefficient ($\sigma_s(\lambda)$) was measured by a 3 wavelength nephelometer (TSI Inc., model 3563) operating at 450, 550, and 700 nm. The instrument has been extensively described in Anderson *et al.* [1996]. The nephelometer receives regular calibration and maintenance according to the standard NOAA/ESRL/GMD network protocols. During the campaign, data were acquired at 1 min resolution at a 30 L min^{-1} flow rate.

The particle volume absorption coefficient ($\sigma_a(\lambda)$) was measured by a Continuous Light Absorption Photometer (CLAP), developed by NOAA/ESRL/GMD. The CLAP is a filter-based instrument that measures light absorption by particles at three wavelengths (428, 528, and 652 nm). Particles are collected on a filter, and light transmission through the filter is monitored continuously. The CLAP has eight sample spots, which are controlled by a solenoid switcher changing to the next sample spot once the transmittance reaches 0.7. During the campaign, the CLAP operated at 1 min time resolution and at a flow rate of 1 L min^{-1} .

Both the nephelometer and the CLAP were operated behind a rack-mounted switched impactor drawer designed by NOAA [e.g., Sheridan *et al.*, 2001] to estimate the size segregated optical properties. The aerosol sample always went through a $10 \mu\text{m}$ impactor in the drawer. Every 6 min an automated valve switched the flow so that it also passed through a $1 \mu\text{m}$ impactor; thus, the nephelometer and CLAP sampling alternated between sub- $1 \mu\text{m}$ and sub- $10 \mu\text{m}$ aerosols.

For the duration of the Dust-ATTACK campaign, additional measurements of the aerosol mass concentration were performed through a certified PM_{10} sampling head (Rupprecht & Patashnick Co., Inc.) using a Tapered Element Oscillating Microbalance (TEOM, Thermo Fisher Scientific, model 1405-F) equipped with a Filter Dynamic Measurement System (FDMSTM). An isokinetic flow splitter is used in combination with an automatic flow controller to divide the main/bypass flow into two components after the air stream passes through the size-selective PM_{10} inlet. The two sample flow components are the main flow (3 L min^{-1}) that flows to the TEOM mass transducer and the bypass flow (13.67 L min^{-1}). The FDMS provides a representative determination of the particulate matter (PM) mass concentration as it exists in the ambient air. The FDMS unit automatically generates mass concentration values M_c ($\mu\text{g m}^{-3}$) that account for both nonvolatile and semivolatile PM components.

To accomplish this, the FDMS unit constantly samples ambient air, and using a switching valve to change the path of the sample flow automatically compensates for the semivolatile fraction of the collected sample. Every 6 min the switching valve alternates the sample flows between the base and reference sample periods. During the base period, sample is collected normally and the base mass concentration is determined. During the reference period, the flow is diverted through a chilled filter to remove the nonvolatile and retain the semivolatile PM. Because of the ambient conditions of high temperature and humidity, the chiller was maintained at a temperature of 10°C to prevent condensation in the chiller during instrument operation. The FDMS system updates a 1 h average of the results every 6 min.

2.2. Aerosol Data Analysis

Aerosol data presented in this paper (mass concentrations, particle size distribution, scattering, backscattering, and absorption coefficients) are reported at standard temperature and pressure conditions (273.15 K and 1013.25 hPa).

2.2.1. Particle Number Size Distribution and Data Reduction

The particle number size distributions measured by the SMPS in the range 11.8–593.5 nm were corrected by the instrument software for the diffusion losses of particles in the SMPS tubing, the contribution of multiply charged particles and the dilution of the aerosol flow before entering the CPC.

The SMPS measures the number distribution in terms of electrical mobility diameter (d_{pm}). The knowledge of the dry dynamic shape factor χ_{dry} , characterizing the behavior of the three-dimensional particle in flow stream, is necessary to convert the SMPS measurements to the sphere-equivalent particle geometric diameter (d_{pve}) according to equation [Hinds, 1999]

$$d_{pm} = d_{pve}/\chi_{dry} \quad (1)$$

The factory calibration of the GRIMM OPC instrument uses monodisperse polystyrene latex spheres whose complex refractive index \tilde{n} is equal to $1.59-0i$ at 655 nm. The conversion of the sphere-equivalent optical diameters (d_{oe}) to d_{pve} must take into account the refractive index of the ambient aerosol [Liu and Daum, 2000; Collins et al., 2000]. The complex refractive index for ambient aerosol was assumed to be $1.53-0.002i$, in the range of values recently published in the open literature for mineral dust in source region [Osborne et al., 2008; Schladitz et al., 2009; Weinzierl et al., 2009; Petzold et al., 2009; McConnell et al., 2010; Formenti et al., 2011; Chen et al., 2011; Ryder et al., 2013a]. Variations of both the real and the imaginary parts in the range indicated by those measurements (1.40–1.56 for the real part and 0.001–0.003 for the imaginary part) have not proven significant in altering the correction factor to be applied to the calibration sphere-equivalent optical diameter values relative to the uncertainties in the estimation of the refractive index and uncertainties due to Mie resonance oscillations of the calculated scattering intensities.

Reconciling the SMPS and the OPC observations during dust events required setting the dry dynamic shape factor χ_{dry} to values in the range 1.2 ± 0.09 as expected for randomly oriented elongated particles [Hinds, 1999]. Various measurements have suggested that mineral dust consists of spheroid-like particles of median two-dimensional aspect ratio in the range 1.4–1.7 [Okada et al., 2001; Chou et al., 2008; Kandler et al., 2009] and height-to-width ratio of the order of 0.3 [Okada et al., 2001; Chou et al., 2008]. Oblong particles will orient along their long axes when flowing in the airstream of the GRIMM OPC. Because the laser beam is perpendicular (but in the same plane) to the airflow direction, the GRIMM OPC may overestimate the cross-sectional size of dust particles, whereas, because of the boundary of the scattering sensing volume, the effect of particle nonsphericity might cancel out. For large particles the counting statistics errors are large, and in the absence of a good estimate of the three-dimensional particle shape distribution, corrections to the scattering intensities due to particle shape have been neglected. One should note also that this has been the choice of most of the studies dealing with particle size distribution of mineral dust [Weinzierl et al., 2009, 2011; Chen et al., 2011; Ryder et al., 2013a], so this assumption facilitates the comparison of results with previous literature.

2.2.2. Parameterization of Size Distributions

The number size distributions obtained by the combination of the SMPS and the OPC instruments have been parameterized by fitting multimodal lognormal distributions [Hinds, 1999] according to the following equation

$$\frac{dN}{d\log r} = \sum \frac{N_{tot}}{\sqrt{2\pi} \log \sigma_g} \exp\left(-\frac{(\log D_p - \log D_g)^2}{2 \log^2 \sigma_g}\right) \quad (2)$$

where the total aerosol number concentration (N_{tot}), the median diameter (D_g), and the geometric standard deviation (σ_g) describe each mode of the aerosol size distribution. It turned out that three to four modes were needed for an adequate representation of the observed dust size distributions. The quality of the lognormal fit was controlled by computing the equivalent mass concentration in the PM_{10} fraction measured by the TEOM analyzer.

The parameterized lognormal size distributions were then used to estimate the dust effective diameter D_{eff} , defined as

$$D_{eff} = \frac{\int D_p^3 \frac{dN}{d\log D_p} d\log D_p}{\int D_p^2 \frac{dN}{d\log D_p} d\log D_p} \quad (3)$$

2.2.3. Aerosol Optical Properties

The highest source of uncertainty in the scattering measurements is the truncation correction related to the geometric restriction of the scattering sensing volume of the nephelometer, limited to 7–170° scattering range instead than 0–180° as nominal [Anderson et al., 1996]. This causes an underestimate of the scattering and the backscattering coefficients, mostly in the supermicron and to a lesser extent in the sub-1 μm size range. Edited

scattering data from NOAA routinely have the truncation corrections described in *Anderson and Ogren* [1998] applied. This algorithm underestimates the truncation correction for aerosols with a dominant coarse mode, such as mineral dust. Here raw data were used instead, and the correction factors accounting for the truncation of the sensing volume have been calculated from the experimentally determined size distribution for a range of values of the complex refractive indices around $1.53-0.002i$, and assuming homogenous-spherical particles. Calculations were performed using the Mie code of *Bohren and Huffman* [2007].

Likewise, the CLAP is operated according to the standard NOAA/ESRL/GMD network protocols. The corrections necessary to pass from the measured attenuation coefficient to the aerosol absorption coefficient σ_a (λ) include accounting for the fraction of light scattered out of the field of view of the detector, erroneously interpreted as absorption, as well as variation in the flow rate and in the spot size. The CLAP was specifically designed to be similar to the Radiance Research Particle Soot Absorption Photometer (PSAP); and thus, PSAP corrections as described in *Bond et al.* [1999] and *Ogren* [2010] are applied.

The nephelometer and the CLAP measure the spectral scattering and absorption coefficients (σ_s and σ_a , respectively). These measurements can be combined to estimate the single-scattering albedo ω_0 as

$$\omega_0 = \frac{\sigma_s}{\sigma_s + \sigma_a} \quad (4)$$

To match the wavelengths, the σ_a values measured at 467, 528, and 652 nm have been logarithmically extrapolated using the absorption Ångström exponent to 450, 550, and 700 nm where the nephelometer operates.

Additionally, the measured σ_s and σ_a in the 10 μm fraction have been combined with the measured PM_{10} mass concentration to provide with the mass scattering and absorption specific efficiencies (MSE and MAE, respectively) defined as

$$\text{MSE, MAE} = \frac{\sigma_{s,a}}{M_c} \quad (5)$$

The mass extinction efficiency (MEE) is then calculated as the sum of MSE and MAE.

To validate these estimates, optical calculations of the spectral σ_s and σ_a values and derived quantities (ω_0 , σ_s , and σ_a , respectively) have been performed using the measured number size distributions leaving the complex refractive index as a free parameter.

2.3. Ancillary Measurements and Products

Additional gas phase and meteorological measurements, as well as ground-based remote sensing observations conducted at the site are listed in Table 1. For the duration of the intensive campaign only, gas phase sampling was performed from a Teflon tube (6 mm diameter), whose intake was located at approximately 2 m above the roof of the sampling station.

The mixing ratio of CO and CO_2 was measured by a 1 Hz laser-based cavity ring-down spectrometer (Picarro, model 3202). Data were acquired every 2 s and averaged every 5 min to achieve a precision of 2 ppb on CO. Ozone mixing ratios were measured with UV Photometric Analyzer (Environmental SA, model O342M). The instrument was operated at 1 L min^{-1} through a 5 μm polytetrafluoroethylene (PTFE) filter in order to prevent aerosols in the air stream to enter the sensing volume. At an averaging time of 10 min, the instrument has a detection limit of 1 ppb. The zero level was performed daily as part of the routine operations. Nitrogen oxides ($\text{NO}/\text{NO}_2/\text{NO}_x$) were measured by means of an UV Chemiluminescence analyzer (Environmental SA, model AC32M). The instrument uses a 5 μm PTFE filter to eliminate aerosol in the air stream, and it was operated at 0.66 L min^{-1} and a sampling rate of 10 min. All instruments were calibrated in the laboratory prior deployment and postdeployment in the field.

The CPR station is also equipped with a standard weather station (Davis Model 6160C, Vantage Pro weather station), providing wind direction, wind speed, air temperature, and relative humidity time series at 9 m above ground level. To fill data gaps due to malfunctions of the weather station, additional measurements acquired from the NOAA National Weather Service station at the San Juan International Airport (located 50 km northeast of CPR) are also considered.

Measurements of the spectral aerosol optical depth (AOD) and column-integrated optical properties are available as part as the AERONET (AERosol RObotic NETwork) program [*Holben et al.*, 2001]. Cloud-screened,

quality-assured level 2.0 data are used in this paper. Fifty-one inversions of the column-averaged volume size distribution from level 2 Sun photometer data by the version 2 inversion algorithm [Dubovik *et al.*, 2006] are available for the field campaign period.

2.4. Dust Emission and Transport to the Caribbean

In addition to the measurements described above, Saharan dust emissions and long-range transport over the Atlantic Ocean during the Dust-ATTACK intensive campaign period are analyzed using numerical simulations of Saharan dust emission and atmospheric aerosol information derived from satellite observations, as well as analysis of model air mass trajectories. This information is used to link the observations to source region and residence time in the atmosphere.

Dust emissions on a domain extending from 12°N to 38°N and 18°W to 40°E, and including the North African dust sources, have been computed using the dust production model developed by *Martcorena and Bergametti* [1995]. This model describes the dust emission processes, i.e., the erosion threshold, the saltation flux, and the dust emission efficiency, as a function of the surface properties (surface roughness length, soil size distribution, and soil texture) and of the wind friction velocity [Martcorena *et al.*, 1997; Laurent *et al.*, 2008]. The emission model is forced by surface wind fields from the European Centre for Medium Weather Forecast.

The Ozone Monitoring Instrument (OMI) aboard the EOS-Aura platform allows retrieval of daily aerosol indexes (AI), with level 3 products delivered for timestamp 12:45 h (GMT) with a 1° × 1° grid resolution. OMI AI products and application fields are presented in *Torres et al.* [2007] and are used here to track long-range transport of dust over the North Atlantic. AI values from the OMI precursor, the Total Ozone Mapping Spectrometer sensor, have been used extensively to characterize the dust sources over the Sahara [Engelstaedter *et al.*, 2006; Prospero *et al.*, 2002; Washington *et al.*, 2003] and to study dust transport variability with regional climate over the North Atlantic [Chiapello and Moulin, 2002; Chiapello *et al.*, 2005]. The AI is able to provide valuable information on the dust plume features over both continent and ocean, although the absolute AI values are a function of plume height [Deroubaix *et al.*, 2013; Ginoux and Torres, 2003].

In order to follow air mass transport from the North Africa to the Caribbean, 10 day back trajectory calculations are performed with the HYSPLIT (Hybrid Single-Particle Lagrangian Integrated Trajectory) model using the Global Data Assimilation System (<http://www.arl.noaa.gov/HYSPLIT.php>) meteorological input data.

3. Results

3.1. Overview of Weather and Air Mass Type During the Field Campaign

The climate in Puerto Rico is tropical, and easterly trade winds prevail during much of the year. During the summer, in particular, the island experiences winds from the east, northeast, or southeast about 60% of the time [Pico, 1974]. Surface pressure waves (easterly waves) that originate off the west coast of Africa and propagate in the tropical trade belt [Thornicroft and Hodges, 2001] are responsible for most of the rainfall in Puerto Rico, although cold fronts, which penetrate to the eastern Caribbean from December to April (winter period), can occasionally bring much rain [Malmgren and Winter, 1999]. Easterly waves are primarily summertime phenomena (typically from May through November) and occasionally can develop into depressions, tropical storms, and hurricanes [Dunkerton *et al.*, 2009].

The wind direction, wind speed, air temperature, and relative humidity time series recorded at CPR and at the NOAA/National Weather Service (NWS) station at San Juan International Airport (SJU) during the campaign are shown in Figure 2. Despite the urban station of SJU cannot, strictly speaking, be considered as a proxy for CPR, there is generally good correspondence between meteorological time series for the two locations. The typical summer weather regime can be recognized over most of the campaign, with persistent moderate easterly winds and an obvious diurnal cycle for temperature and, to a lesser extent, relative humidity, indicating a prevalence of fair and dry weather. During 4 and 5 July, a vigorous tropical wave affected the island, leaving rainfall accumulations ranging from 50 to 100 mm, as well as gusty winds. This is well documented by the temperature drop and wind shifts observed by the two stations in those days. After that disturbance, a generally fair and mainly dry weather pattern prevailed with limited afternoon convection focused mostly across western Puerto Rico each day.

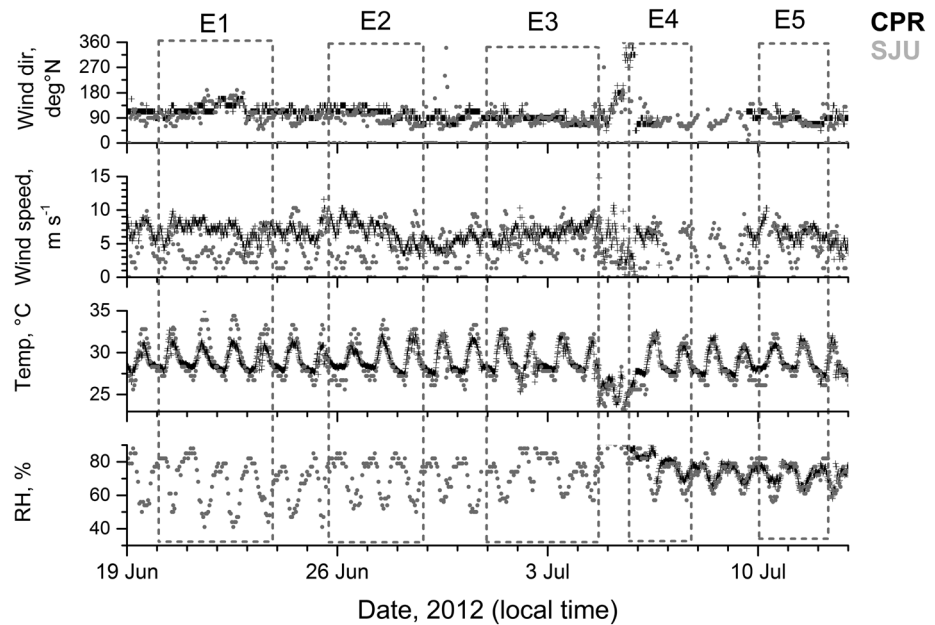


Figure 2. (top to bottom) Wind direction, wind speed, air temperature, and relative humidity, respectively. Time series recorded by the CPR station (black points) and the NOAA station of San Juan International Airport (grey points) from 23 June to 13 July 2012.

There is no significant deviation with respect to the long-term climatology during the campaign period in terms of sea level pressure and 1000 mb vector wind composite anomalies obtained from the National Center for Environmental Prediction (NCEP)/National Center for Atmospheric Research Reanalysis (Figure 3). A slight negative anomaly for pressure is found throughout the Caribbean region, while the low-level wind velocity is very close to the long-term average. According to the NWS Monthly Climate Reports for Puerto Rico [NWS, 2012], June 2012 was the warmest and driest June on record, especially for the first half of the month, with a positive temperature anomaly at San Juan of 1.3°C and a total rainfall of only 4 mm, whereas the 1981–2010 average is about 110 mm.

Five dust events (E1 to E5) were detected during the campaign. These events corresponded to increases of the aerosol mass concentration M_c above $20 \mu\text{g m}^{-3}$ and up to $70 \mu\text{g m}^{-3}$ in the PM_{10} for a duration of 2 to 4 days and alternated with background periods lasting 1 to 2 days (Figure 4). The increase in mass concentration corresponded to an increase of the measured spectral scattering and absorption coefficients σ_s and σ_a .

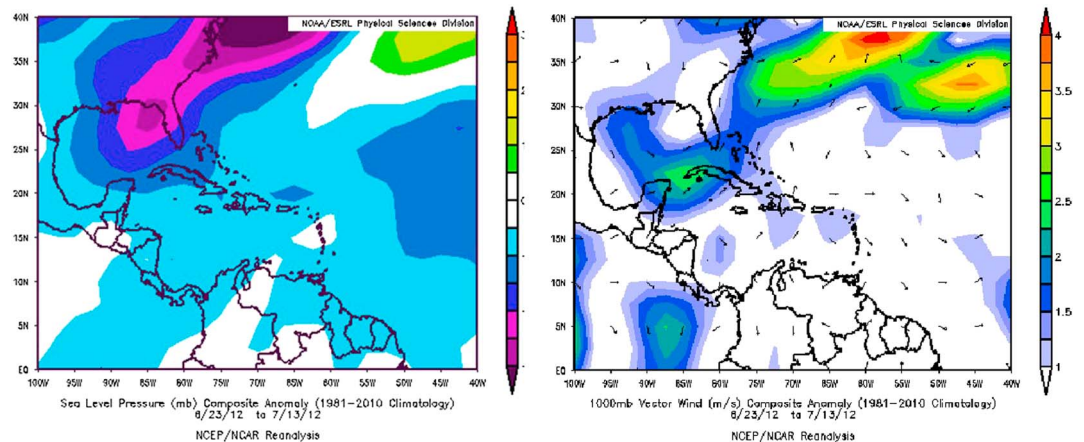


Figure 3. (left) Sea level pressure and (right) 1000 mb vector composite anomalies with respect to the 1981–2010 climatology obtained from the NCEP/NCAR Reanalysis (images provided by the NOAA/ESRL Physical Sciences Division, Boulder, Colorado, from their web site at <http://www.esrl.noaa.gov/psd/>).

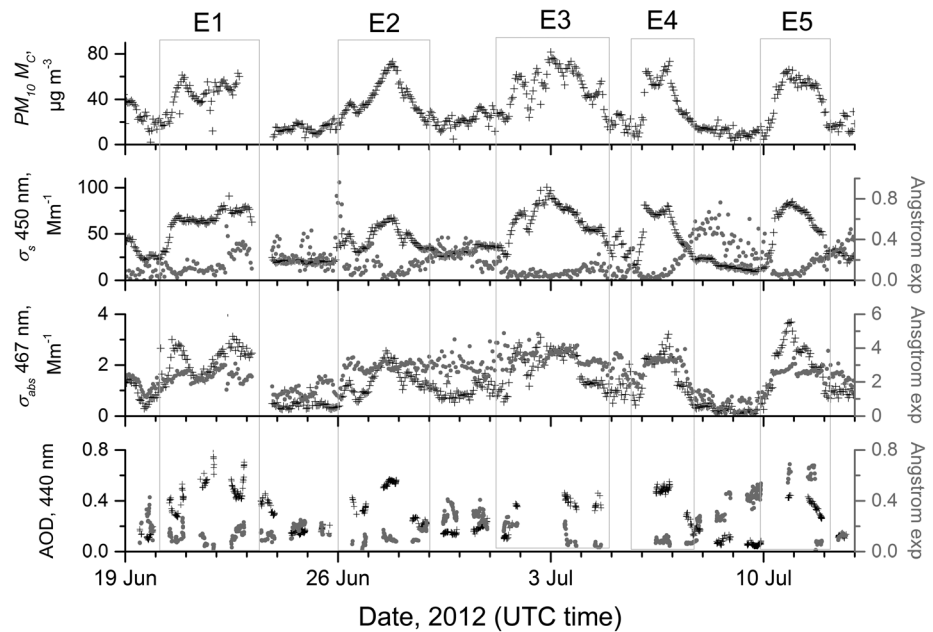


Figure 4. (top to bottom) Time series of (i) aerosol mass concentration M_c ($\mu\text{g m}^{-3}$); (ii) spectral scattering coefficient σ_s (black crosses) and its spectral dependency (scattering Ångström exponent, grey dots); (iii) spectral absorption coefficient σ_a (black crosses) and its spectral dependency (absorption Ångström exponent, grey dots); and (iv) the aerosol optical depth at 440 nm (black crosses) and its spectral dependence (Ångström exponent, grey dots). The mass concentration and scattering/absorption coefficients refer to the PM_{10} fraction of the aerosol.

in the PM_{10} fraction (also shown in Figure 4). There was also a systematic enhancement of the aerosol optical depth (AOD), which peaked at 0.78 and 440 nm during the episode (E1). During these events, the PM_1 fraction accounts for 20–25% of the PM_{10} scattering coefficient at 450 nm, and between 10 and 15% at 700 nm, suggesting up to 90% of the scattering is due to the supermicron fraction. During these events the supermicron absorption accounts for 30–40% of the PM_{10} absorption coefficient at all wavelengths. Because this is a marine site, these size fractionations are not much different from normal (nondust event) values of PM_1 fractions for scattering and absorption (20 and 60%, respectively) despite the enhanced loading due to dust.

The temporal correlation between the surface measurements (σ_s , σ_a , and M_c) and the column AOD, as well as that of their spectral dependence, suggest that if there was transport of dust outside the marine boundary layer (MBL) during the field campaign, it did not occur in a separate air mass but rather in a plume extending from the MBL to above. In summertime, the transatlantic transport of mineral dust occurs mostly in the Saharan Air Layer (SAL), an intrusion of dry and warm air in the free troposphere originating over the Sahara and extending, almost undisturbed, across the Atlantic [Karyampudy *et al.*, 1999]. We found that the ratio between the AOD and the surface extinction coefficient (estimated as the sum of σ_a and σ_s), a measure of the scale height of the dust layer, remained practically constant during the dust events ($h \sim 5000\text{--}5500\text{ m}$), suggesting consistency in the dust vertical profile. The derived scale height is consistent with the expected top height of the SAL determined from the strong temperature inversions in the radiosonde data at San Juan (available online at <http://weather.uwyo.edu/upperair/sounding.html>) as well as with the vertical profiles of dust sounded by the spaceborne lidar CALIOP (Cloud-Aerosol Lidar with Orthogonal Polarization, available online at <http://www.icare.univ-lille1.fr/calipso/browse/>). During episode E5, the column scattering Ångström exponent increased to 0.6, whereas the surface scattering Ångström exponent remained below 0.2, suggesting that the upper dust layer might have been mixed with fine particles other than dust. The variability of dust vertical profiles has previously been pointed out by Reid *et al.* [2002] who illustrated situations when dust was more abundant in the MBL below the trade wind inversion and situations when the dust transport occurred exclusively in the SAL above the MBL.

Figure 5 shows the time series of the NO , NO_2 , O_3 , CO , and CO_2 mixing ratios and the number concentration of submicron particles (N_{sub}) measured by the SMPS. Background values of CO were around 30–40 ppb and

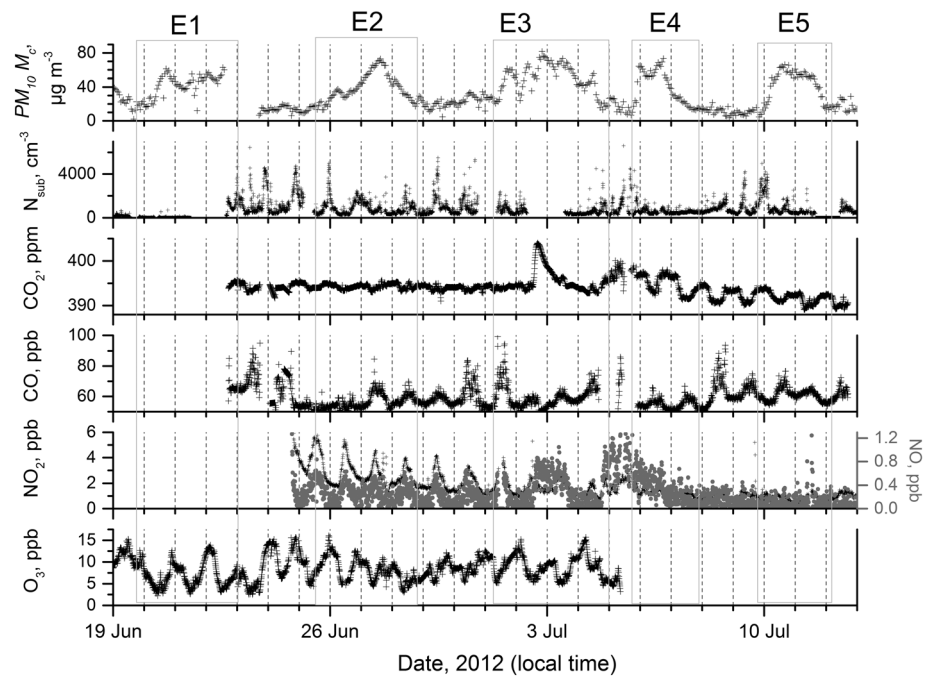


Figure 5. (top to bottom) Time series of (i) aerosol mass concentration M_c in the PM_{10} fraction ($\mu g m^{-3}$); (ii) number concentration of submicron particles (N_{sub} , cm^{-3}); (iii) CO_2 mixing ratio (ppm); (iv) CO mixing ratio (ppb); (v) NO (grey dots, ppb, right axis) and NO_2 (black crosses, ppb, left axis) mixing ratios; and (vi) O_3 (ppb) mixing ratio.

~1 ppb for NO_x . A diurnal cycle is observed for these gases with peak values reaching 100 ppb and 7 ppb for CO and NO_x , respectively, during daytime. Typical sources for these gases are anthropogenic emissions, including ship traffic, so their observed variability suggests that polluted air masses episodically but frequently reached the sampling site during the field campaign. In contrast, values of O_3 never exceeded 15 ppb and were maximum at nighttime, in phase with CO_2 mixing ratios, whose daytime to nighttime variability should reflect the oscillation of the boundary layer height. The CO_2 and NO_x mixing ratio tended to decrease after the tropical wave of the 4–5 July. N_{sub} also exhibits a large diurnal variability, although the maximum occurrences are observed both during the day and night. Background (nondust) values of particle concentration N_{sub} were around 300–500 cm^{-3} , which is typical for marine regions [O’Dowd and de Leeuw, 2007]. Peaks in N_{sub} were detected frequently, even during the dust events. The magnitude of N_{sub} peaks, exceeding 500 cm^{-3} , is consistent with previous wintertime (nondust) measurements made at the site [Allan et al., 2008]. These peaks occurred either at nighttime, when they correlated with O_3 maxima, or during daytime around local midday, generally corresponding to peaks in the NO_x ($NO + NO_2$) mixing ratio up to ~5 ppb, and at times with peak values of CO reaching ~100 ppb.

3.2. Characteristics of Individual Dust Events

3.2.1. Source Area Attribution

The source area and the long-range transport of the dust plumes over the North Atlantic Ocean observed during the field campaign (E1 to E5, Table 1 and Figure 4) was analyzed by visual inspection and collocation of model air mass trajectories, OMI EOS-Aura satellite observations, and emission simulation by the dust production model. Results are shown in Figures 6 and 7. The dust events reached Puerto Rico after typically 6 to 8 days of transport. The E1 dust event corresponds to emissions on 13–16 June occurring in two distinct source areas of the Sahara, indicated as E1a and E1b in Figure 6. After emission, the E1a and E1b plumes remained distinct and reached Puerto Rico between 20 June and 23 June. E2 corresponds to Saharan dust emitted on 18–20 June, the plume reaching the Puerto Rican coast on 27 June. E3 also corresponds to two different activated source areas, E3a and E3b, between 22 and 25 June. These events reach Puerto Rico between 1 and 3 July. E4 and E5 dust source activations occur on 27–29 June and on 1–3 July, respectively. These two events are observed in Puerto Rico on 6 July and 10–11 July. Timing and dynamics of the dust plumes transport tracked with OMI AI are consistent with 10 day HYSPLIT air mass trajectories.

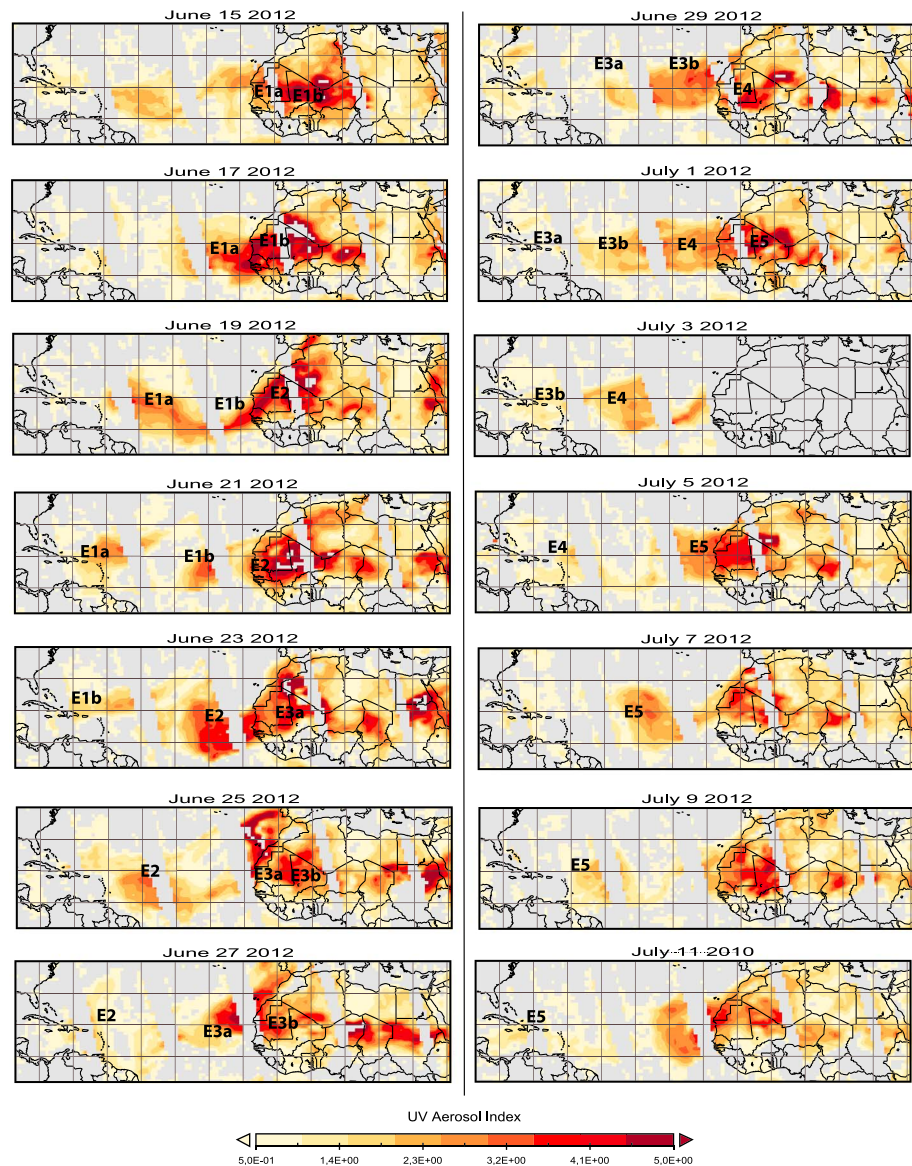


Figure 6. Composite from OMI EOS-Aura satellite observations indicating the evolution of the five dust plumes (E1 to E5) during the field campaign where the plumes are represented by the OMI product UB aerosol index.

OMI AI shows high dust atmospheric concentration over large areas in Mauritania and Western Sahara, Mali, Algeria (south, west, and central) Niger (west and central), and in the Bodelé Depression in Chad. Lower AI values (which we associate to lower atmospheric concentrations) can also occasionally be observed at the borders between Algeria, Morocco, and southern Tunisia, as in Central Libya. The OMI AI product is most sensitive to plumes at altitudes above ~ 1 km: as a consequence, the surface emission location could be misplaced as the plumes are detected not directly at the time of emission but only later when they are at a certain elevation in the atmosphere.

To avoid these biases, the main active Saharan source areas for the five events have also been simulated using the dust production model [Martcorena and Bergametti, 1995]. Emission locations (computed from noontime to noontime) are reported in Figure 7. Although most of the emissions occur in the West Saharan region, changes in the location and relative intensity of the main source areas can be observed from one event to another. For E1a, dust sources are in Mauritania/Western Sahara and in Northwestern Algeria. For E1b, emissions are simulated in Western Sahara, in Mauritania and on the Mauritanian/Malian border, and to a lesser extent in Mali, Northern Niger, and Chad (Figure 7a). Dust emissions are mainly simulated

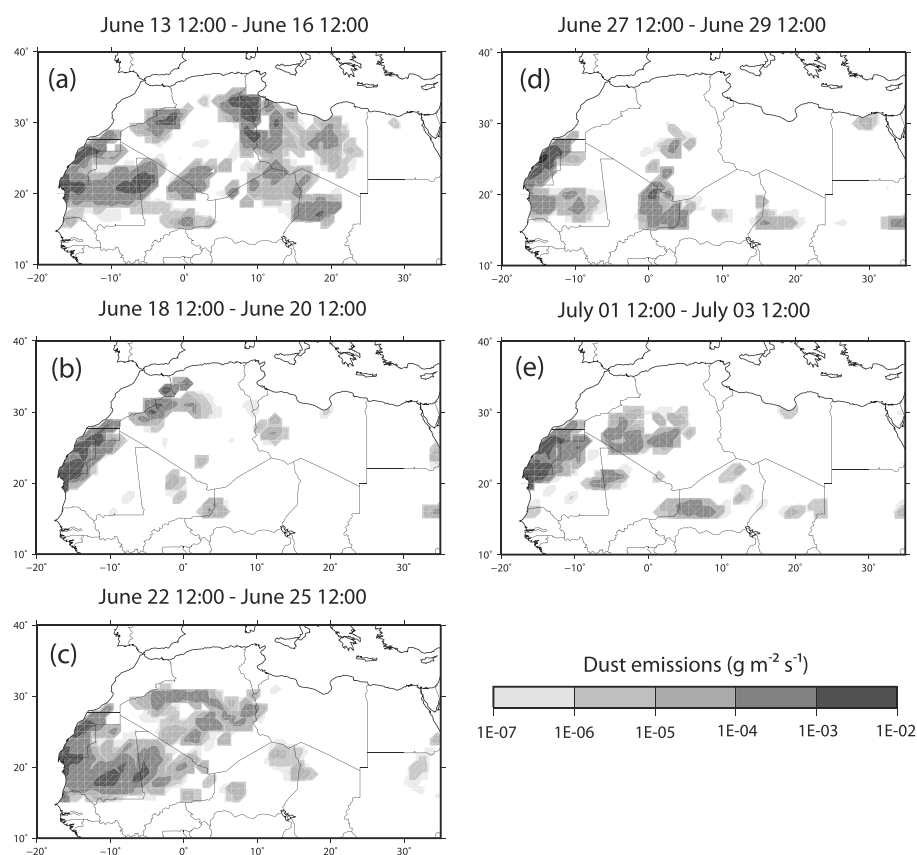


Figure 7. Dust emission fluxes computed from noontime to noontime (in UTC) for periods corresponding to the studied events: (a) E1a and E1b, (b) E2, (c) E3a and E3b, (d) E4, and (e) E5.

in Western Sahara for E2 (Figure 7b). Most of the emissions are simulated in south-central Mauritania and close to the western coast for E3a, whereas emissions located in the Western Sahara, South Mauritania, and Central Algeria are simulated for E3b (Figures 7c). Main sources of dust for E4 are the Western Sahara, South Mauritania, Eastern Mali, and Central Algeria (Figure 7d). During E5, emissions cover large areas in Western Sahara, Northern Mauritania, and Central Algeria. Emissions are also simulated in Eastern Mali and Niger (Figure 7e). There is therefore good correspondence between the OMI observations and the numerical simulations, giving confidence in the identification.

3.2.2. Particle Size Distribution

Table 2 shows the modal parameters of the lognormal fits of number size distributions obtained from the harmonized SMPS/OPC measurements characteristic during dust events. The number size distributions are characterized by three-to-four modes of varying amplitudes but relatively invariant median diameter.

An ultrafine mode below 100 nm is centered most frequently in the 24–58 nm range, although a very few times two additional modes (one below 16 nm and one in the 70–90 nm range) are also present. The nighttime peaks in N_{sub} below 20 nm might indicate new particle formation, which is observed during nighttime in environments such as forested areas dominated by biogenic volatile organic carbon (VOC) emissions [Ortega *et al.*, 2012] or marine areas characterized by iodine emissions [Allan *et al.*, 2015]. We can only be speculative on this phenomenon as we did not measure particles smaller than 10 nm during the field campaign. A number of studies have reported significant concentration of organic particulate matter and nitric/sulfuric acids at Puerto Rico [Novakov *et al.*, 1997; Mayol-Bracero *et al.*, 2001]. Significant concentrations of biogenic precursors for secondary organic aerosols are also emitted in West Africa during the summer season [Capes *et al.*, 2009]. Indeed, a closer look at the chemical composition both in the gas and in the aerosol phases will be needed to explain the nighttime peaks in N_{sub} . The ultrafine mode is unlikely to be related to African dust emissions. Nucleation events induced by mineral dust photochemistry in the presence of SO_2 have been demonstrated [Dupart *et al.*, 2012] but do not seem to be happening in our study.

Table 2. Minimum, Mean, and Maximum Values for the Modal Parameters (in nm) of the Lognormal Fits of Number Size Distributions Characteristic of the Dust-ATTACK Observations During Dust Events

| | | Ultrafine | Accumulation | Coarse |
|------------------|------------|---------------|--------------|-----------|
| Min | D_p | 7/24/70 | 100/200/500 | 1600/3400 |
| | σ_p | 1.2/1.1/1.3 | 1.4/1.2/1.2 | 1.3/1.2 |
| | N_{tot} | 350/40/200 | 80/50/3 | 0.40/0/01 |
| Mean | D_p | 11/42/78 | 162/229/593 | 1903/3815 |
| | σ_p | 1.4/1.5/1.6 | 1.5/1.2/1.4 | 1.4/1.3 |
| | N_{tot} | 663/553/340 | 295/128/12 | 2.1/0.07 |
| Max | D_p | 16/58/90 | 200/280/800 | 2200/4600 |
| | σ_p | 1.5/1.9/1.9 | 2.0/1.3/1.6 | 1.5/1.3 |
| | N_{tot} | 1000/3800/400 | 1000/240/25 | 4.0/0.15 |
| # of occurrences | | 4/34/5 | 31/9/35 | 34/26 |

The accumulation mode extends from 100 to 800 nm. It is generally bimodal, with peak mode diameters at 162 and 593 nm. Complementary analysis of the chemical composition shows that the mass fraction of the accumulation mode contributed by mineral dust is of the order of 70% and 20% during and outside the dust outbreaks, respectively (P. Formenti, unpublished data, 2012). This indicates that dust in the accumulation mode remains airborne, albeit at lower concentrations, and thus constitutes a persistent component of the regional aerosol load throughout the summer.

The coarse mode, persistent during and outside dust outbreaks, extends up to 7 μm . It is bimodal, with modal geometric diameters in 1.6–2.2 μm and 3.4–4.6 μm ranges. This second mode, less pronounced than the first, is also less constrained as it often exceeds the limits of the particle size range covered by the in situ measurements. Complementary measurements presented in Denjean *et al.* [2016] indicate that mineral dust represented a relatively uniform fraction of this mode (70–80%) during and outside dust outbreaks.

Figure 8 shows examples of the combined volume size distributions ($dV/d\log D$) from the SMPS and OPC, normalized to the total volume, for the five dust events observed during the field campaign. For comparison, results obtained during background periods (29 June to 1 July 2012; 7–9 July; and 11–13 July) are also shown. Due to the limited variability of the position and the relative magnitude of the modes from one episode to

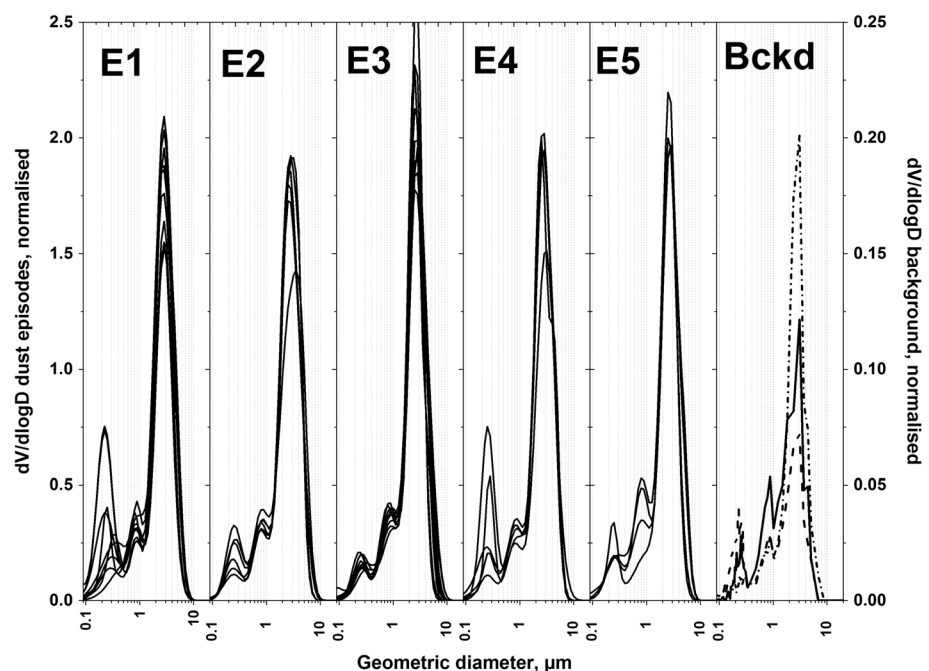


Figure 8. Examples of the volume size distributions ($dV/d\log D$) from SMPS and GRIMM, normalized to the total volume, for the five dust events observed during the field campaign. For comparison, results obtained during background periods (29 June to 1 July 2012; 7–9 July; and 11–13 July) are also shown.

Table 3. Mean and Standard Deviations for the Spectral Single-Scattering Albedo ω_0 (PM₁₀ and PM₁ Fractions) for the Five Dust Outbreaks (E1 to E5) During the Dust-ATTACK Experiment

| | Dp < 10 μm | | | Dp < 1 μm | | |
|--------------------|-----------------------|---------------|---------------|----------------------|---------------|---------------|
| | 428 | 528 | 428 | 528 | 428 | 528 |
| E1 | 0.968 (0.006) | 0.976 (0.005) | 0.985 (0.004) | 0.943 (0.014) | 0.944 (0.014) | 0.949 (0.016) |
| E2 | 0.971 (0.005) | 0.979 (0.003) | 0.988 (0.002) | 0.954 (0.011) | 0.958 (0.010) | 0.967 (0.010) |
| E3 | 0.972 (0.005) | 0.980 (0.003) | 0.991 (0.002) | 0.957 (0.015) | 0.962 (0.014) | 0.972 (0.015) |
| E4 | 0.969 (0.003) | 0.978 (0.003) | 0.989 (0.001) | 0.953 (0.010) | 0.958 (0.008) | 0.970 (0.008) |
| E5 | 0.965 (0.003) | 0.974 (0.002) | 0.985 (0.001) | 0.946 (0.009) | 0.952 (0.008) | 0.963 (0.007) |
| Mean dust episodes | 0.969 (0.065) | 0.976 (0.065) | 0.984 (0.066) | 0.95 (0.07) | 0.95 (0.07) | 0.96 (0.07) |
| Background | 0.977 (0.01) | 0.980 (0.01) | 0.985 (0.01) | 0.953 (0.04) | 0.948 (0.05) | 0.942 (0.06) |

the next, the effective diameter D_{eff} is on average $2.5 \pm 0.1 \mu\text{m}$, during both dust and background conditions. This can also be explained by the fact that sea salt concentrations represent a constant background of the order of 20–25% of the estimated mass in all conditions. The shape and extent of the measured volume size distributions are consistent with all independent measurements made at the site, for example, the comparison of the total mass concentration estimated from the measured number size distributions to that measured by the TEOM yields a linear correlation ($R^2 = 0.80$). The regression line forced through zero yields a slope of 0.95 (± 0.03) if a particle mass density value of 2.65 g cm^{-3} is used. The measured volume size distributions also allow reproduction of both the particle scattering and absorption coefficients in optical closure calculations when realistic values of the complex refractive indexes are used (see section 3.2.3).

3.2.3. Dust Optical Properties

The scattering and absorption coefficients can be used to estimate the single-scattering albedo ω_0 of mineral dust. In conjunction with the measured mass concentration M_c , the mass scattering and absorption efficiencies in the PM₁₀ fraction (MSE and MAE, respectively) can be calculated. For dust episodes, we isolated data corresponding to values of the mass concentration exceeding $20 \mu\text{g m}^{-3}$. Data below this threshold were considered as corresponding to local background. In the absence of a direct measurement of submicron aerosol mass (TEOM measures total mass), only an approximate estimate of the MSE and MAE in the PM₁ fraction can be given. To do so, the estimated PM₁ mass concentration from the GRIMM OPC is used assuming a particle density of 2.65 g cm^{-3} . PM₁ mass concentrations range between 10 and $14 \mu\text{g m}^{-3}$ for the dust episodes. The mean and standard deviations of ω_0 , MSE, and MAE for each of the five dust outbreaks and their overall mean and standard deviation, both in the PM₁ and PM₁₀ fractions, are shown in Tables 3–5, respectively.

The mean values of ω_0 range between 0.97 and 0.98 and between 0.94 and 0.96 for the PM₁₀ and PM₁ dust fractions, respectively (Table 3). There is no significant difference among episodes, or among episodes and the mean background values, regardless of the size fraction. There is also very limited spectral dependence for these values.

In contrast, the MSE and the MAE values are more diverse (Tables 4 and 5). At 450 nm, the mean value of MSE is $1.36 (\pm 0.31) \text{ m}^2 \text{ g}^{-1}$ for PM₁₀, and $1.5 (\pm 0.5) \text{ m}^2 \text{ g}^{-1}$ for PM₁. At 428 nm, the mean value of MAE is $0.04 (\pm 0.01) \text{ m}^2 \text{ g}^{-1}$ for PM₁₀ and $0.09 (\pm 0.05) \text{ m}^2 \text{ g}^{-1}$ for PM₁. The spectral dependence of both MSE and MAE is pronounced (see Tables 4 and 5), but their episode-to-episode variability is more accentuated. The large

Table 4. Same as Table 3 but for Mass Scattering Efficiency (MSE, $\text{m}^2 \text{ g}^{-1}$)

| | Dp < 10 μm | | | Dp < 1 μm | | | Dp < 10 μm | Dp < 1 μm |
|--------------------|-----------------------|-------------|-------------|----------------------|-------------|-------------|-----------------------|----------------------|
| | 450 | 550 | 700 | 450 | 550 | 700 | 700/450 | 700/450 |
| E1 | 1.49 (0.31) | 1.44 (0.30) | 1.42 (0.28) | 1.53 (0.51) | 1.12 (0.35) | 0.81 (0.23) | 0.15 (0.10) | 1.43 (0.29) |
| E2 | 1.08 (0.14) | 1.05 (0.13) | 1.04 (0.12) | 1.21 (0.29) | 0.95 (0.23) | 0.76 (0.19) | 0.12 (0.08) | 1.06 (0.27) |
| E3 | 1.29 (0.27) | 1.27 (0.27) | 1.26 (0.26) | 0.92 (0.23) | 0.75 (0.22) | 0.62 (0.21) | 0.08 (0.04) | 0.96 (0.22) |
| E4 | 1.27 (0.14) | 1.24 (0.14) | 1.24 (0.14) | 0.76 (0.06) | 0.60 (0.06) | 0.48 (0.07) | 0.07 (0.06) | 1.06 (0.24) |
| E5 | 1.32 (0.14) | 1.29 (0.15) | 1.27 (0.15) | 1.01 (0.11) | 0.86 (0.12) | 0.71 (0.13) | 0.11 (0.07) | 0.92 (0.22) |
| Mean dust episodes | 1.36 (0.31) | 1.32 (0.30) | 1.29 (0.30) | 1.01 (0.30) | 0.86 (0.20) | 0.67 (0.13) | 0.16 (0.10) | 1.27 (0.36) |
| Background | 1.80 (0.96) | 1.69 (0.91) | 1.63 (0.89) | 2.8 (0.9) | 1.5 (0.8) | 1.2 (0.7) | 0.31 (0.22) | 1.93 (0.66) |

Table 5. Same as Table 3 but for Mass Absorption Efficiency (MAE, $\text{m}^2 \text{g}^{-1}$)

| | Dp < 10 μm | | | Dp < 1 μm | | | Dp < 10 μm | Dp < 1 μm |
|--------------------|-----------------------|---------------|---------------|----------------------|-------------|--------------|-----------------------|----------------------|
| | 428 | 528 | 652 | 428 | 528 | 652 | 652/428 | 652/428 |
| E1 | 0.049 (0.016) | 0.036 (0.013) | 0.022 (0.009) | 0.09 (0.05) | 0.07 (0.05) | 0.05 (0.007) | 2.4 (0.3) | 1.8 (0.3) |
| E2 | 0.033 (0.006) | 0.023 (0.004) | 0.012 (0.002) | 0.06 (0.02) | 0.04 (0.02) | 0.03 (0.002) | 2.9 (0.2) | 2.2 (0.4) |
| E3 | 0.038 (0.009) | 0.026 (0.007) | 0.012 (0.003) | 0.04 (0.02) | 0.03 (0.01) | 0.02 (0.002) | 3.5 (0.4) | 2.4 (0.5) |
| E4 | 0.041 (0.004) | 0.028 (0.003) | 0.014 (0.002) | 0.04 (0.01) | 0.03 (0.01) | 0.02 (0.001) | 3.3 (0.2) | 2.4 (0.3) |
| E5 | 0.048 (0.007) | 0.034 (0.005) | 0.020 (0.003) | 0.06 (0.02) | 0.05 (0.01) | 0.03 (0.002) | 2.7 (0.2) | 2.1 (0.2) |
| Mean dust episodes | 0.037 (0.013) | 0.027 (0.010) | 0.015 (0.007) | 0.06 (0.02) | 0.04 (0.02) | 0.03 (0.01) | 2.9 (0.8) | 2.0 (0.7) |
| Background | 0.043 (0.036) | 0.035 (0.029) | 0.025 (0.021) | 0.09 (0.07) | 0.07 (0.05) | 0.05 (0.04) | 1.8 (0.9) | 1.5 (0.7) |

standard deviation around the mean MSE and MAE values for episodes E1 and E3 might reflect the fact that those episodes were the result of successive plumes with differing source regions (Figures 6 and 7). Furthermore, there is a significant difference between values of MSE and MAE obtained for dust and background conditions: for background cases the mean MSE varies between $1.8 (\pm 0.9) \text{m}^2 \text{g}^{-1}$ for PM_{10} and $2.8 (\pm 0.9) \text{m}^2 \text{g}^{-1}$ for PM_1 at 450 nm, whereas MAE ranges between $0.04 (\pm 0.04) \text{m}^2 \text{g}^{-1}$ for PM_{10} and $0.09 (\pm 0.07) \text{m}^2 \text{g}^{-1}$ for PM_1 . These variations in the MSE values, both for the PM_{10} and the PM_1 fractions, could be related to the relative proportions of the fine and coarse modes. Values of the mass extinction efficiency (MEE, $\text{m}^2 \text{g}^{-1}$) for dust are of the order of $1.1\text{--}1.4 \text{m}^2 \text{g}^{-1}$ at 450 nm for the PM_{10} and the PM_1 fractions, respectively.

To validate these observations, values of MSE, MAE, and ω_0 in the PM_{10} fraction at three wavelengths have also been estimated using Mie theory assuming homogeneous spherical particles. Optical calculations using the measured number size distributions as input agree with the measured optical properties within 10% (not shown). For wavelengths at or below 550 nm, the best agreement is obtained for values of the complex refractive index of $1.53\text{--}i0.002$, whereas the imaginary part tends to lower values (0.001) at 652/700 nm. These values are comparable with those obtained for mineral dust in western and northern Africa [Formenti *et al.*, 2001; Ryder *et al.*, 2013a]. Moreover, a negative wavelength dependence of the imaginary part of the dust refractive index was also observed by Schladitz *et al.* [2009] in source region.

Our values of ω_0 for PM_{10} dust at CPR are consistent with the measurements of Ryder *et al.* [2013a] for Saharan mineral dust at short time after emission (<3 days) in the SAL outflow, as well as with values reported by Jeong *et al.* [2008] for dust offshore western Africa (MSE between 0.9 and $1.21 \text{m}^2 \text{g}^{-1}$ and ω_0 between 0.9 and 0.96 at 550 nm). In contrast, the PM_1 ω_0 during Dust-ATTACK is lower than previous estimates of the fine mode for dust over source regions [e.g., McConnell *et al.*, 2008; Osborne *et al.*, 2008], although Ryder *et al.* [2013a] reported a large range of variability (0.91–0.99) from the FENNEC experiment. This result suggests that the absorbing properties of the dust plumes in the PM_1 fraction evolved during transatlantic transport. This behavior was also observed for dust transported in the Amazonia by Formenti *et al.* [2001] who reported PM_{10} ω_0 in the range 0.92–0.95. Lower MEE values in the PM_{10} dust fraction ($0.39 \text{m}^2 \text{g}^{-1}$) were reported by Ryder *et al.* [2013b] in the SAL outflow over the source region, which could be explained by a higher contribution of fine particles to the dust population at Puerto Rico since smaller particles have enhanced absorption and scattering efficiency per unit mass.

4. Discussion

In recent times, a number of studies have investigated the size distribution of African mineral dust at various time during transport, pointing out that a significant fraction of particles larger than $10 \mu\text{m}$ can be found airborne over large distances, despite gravitational settling [Maring *et al.*, 2003a; Reid *et al.*, 2003b, 2008; Weinzierl *et al.*, 2009, 2011; Müller *et al.*, 2010; Ryder *et al.*, 2013a, 2013b].

In order to provide further insights on the evolution of dust plumes with distance from source, Figure 9 shows a comparisons of dust volume size distribution (i) measured in situ, at surface level, in the source region at emission (i.e., during an erosion episode), then 1 and 2 days later [Formenti *et al.*, 2014]; (ii) surface in situ [Müller *et al.*, 2010] and column-integrated data at the beginning of transport across the Atlantic 1 to 3 days after emission at the surface Cape Verde Atmospheric Observatory (CVAO), approximately 900 km toward the

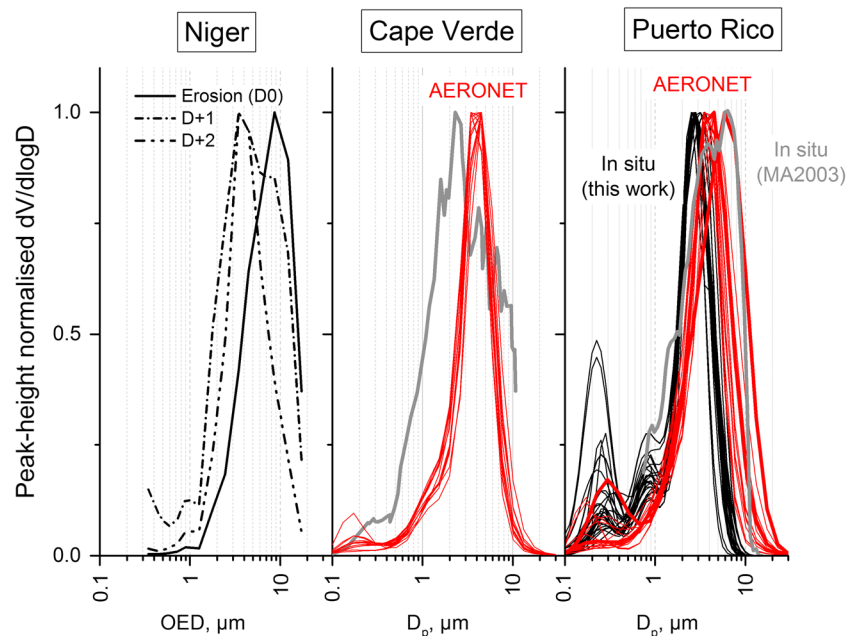


Figure 9. Comparison of peak-height normalized volume distributions: (i) measured in situ, at the surface level, over the source region at emission (i.e., during an erosion episode), then 1 and 2 days later [Formenti *et al.*, 2014]; (ii) surface in situ [Müller *et al.*, 2010] (grey line) and column-integrated AERONET data (red line) at the beginning of transport across the Atlantic 1 to 3 days after emission at the surface Cape Verde Atmospheric Observatory (CVAO), approximately 900 km toward the coast of West Africa (Mauritania and West Sahara); (iii) surface in situ (blank lines) and AERONET column-integrated data (red lines) during Dust-ATTACK and PRIDE (this work and Maring *et al.* [2003a]; grey line), over Puerto Rico, at the far end of transport over the North Atlantic Ocean. Note that D_p represents aerodynamic or geometric diameter, whereas OED represents optical equivalent diameter obtained by optical counters or Sun photometers.

coast of West Africa (Mauritania and West Sahara); and (iii) surface in situ and column-integrated data during Dust-ATTACK and PRIDE (this work and Maring *et al.* [2003a]), over Puerto Rico, at the far end of transport over the North Atlantic Ocean.

Figure 9 shows that volume of dust aerosols is primarily in the 1–10 μm size bin, regardless of time after emission. Measurements over Niger, western Africa, illustrate that the modal peak diameter, expressed as optical equivalent diameter (OED), evolves rapidly within the first 2 days after emission from $\sim 9 \mu\text{m}$ to $\sim 4.5 \mu\text{m}$ (Figure 9, left panel, adapted from Formenti *et al.* [2014]). Following short-range transport to Cape Verde, the modal peak diameter of the volume size distribution obtained with in situ measurements is found in the range 2–3 μm (geometric equivalent), and larger particles (i.e., diameters $> 8 \mu\text{m}$) are depleted [Müller *et al.*, 2010]. For the same time period, the modal peak diameter of the column-integrated size distributions is found around 4.5 μm (OED). For the range of refractive index expected for mineral dust, this should result in a geometrical-equivalent diameter of the order of 8 μm .

Over Puerto Rico, the volume size distributions measured during Dust-ATTACK show little variability in the modal position, peaking at 2–3 μm in geometric diameter. The maximum peak heights in the AERONET size distribution at CPR are found between 3.42 and 4.48 μm (two consecutive midpoints in the logarithmically spaced diameter distributions) in optical equivalent diameter. Again, when correcting for refractive index, these values are equivalent to ~ 6 –8 μm in geometric diameter. There is little variability in the modal peak diameter, despite some changes in the source regions of emission (in particular, during episode E2, when the contribution of Sahelian sources at the border between Mali and Niger dominated), suggesting that large-scale mixing of the dust plumes and size segregation during transport smooth out possible differences related to the origin. The in situ surface values measured at CPR have a modal diameter much lower than reported by Maring *et al.* [2003a] during PRIDE, but very similar to that reported by Formenti *et al.* [2001] for dust over the Amazon forest (not shown).

These observations suggest a number of considerations. First, it looks like the modal diameter remains unvaried from one side to the other of the Atlantic Ocean (e.g., from Cape Verde to CPR), suggesting that

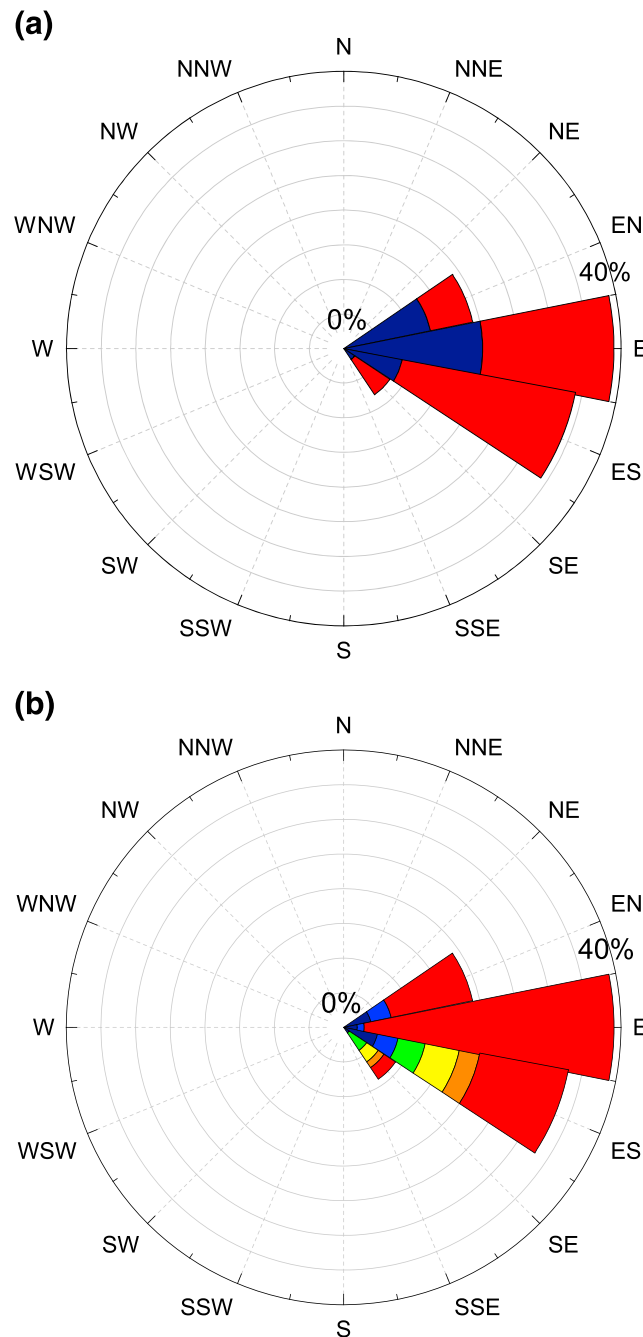


Figure 10. Air mass arrival directions and their relation to (a) the number concentration of submicronic particles at the CPR station during dust events and (b) the single-scattering albedo ω_0 of the PM_{10} fraction at 550 nm.

Subsidence of the dust-laden air mass prior arriving to CPR is indeed observed in the CALIOP data during the field campaign [Denjean *et al.*, 2016]. Liu *et al.* [2008] indicated that the measured dust optical properties remained homogeneous in the vertical in the due course of transport. However, earlier observations above Puerto Rico during PRIDE have shown that the vertical profiles are highly variable with height and that concentrations of large particles might reach a maximum below the trade wind inversion rather than at the surface [Reid *et al.*, 2002; Maring *et al.*, 2003b].

Second, Figure 9 shows a significant peak in submicron particles in the CPR data which is not evident earlier in transport. The CPR site is under the influence of the easterly trade winds and far from major anthropogenic

gravitational settling is practically ineffective after 2–3 days from uplift once the dust plume is over the ocean. However, there is a clear difference between the observations of Maring *et al.* [2003a] and this study, which cannot simply be attributed to differences in the sampling method, showing that at least for some conditions, larger particles ($d > 5 \mu m$) can travel large distances over 6–8 days of transport. Finally, both at Cape Verde and at CPR, we observed that the modal diameter of the column-integrated size distributions is systematically at a higher value than observed at the surface. The AERONET size distributions represent column-integrated values at ambient conditions, while in situ size distributions are measured at ground level at dry conditions ($RH < 40\%$). The correlation between surface and column size distributions might depend on the ambient RH as well as the vertical distribution of aerosols. We disregard an effect related to relative humidity as Denjean *et al.* [2015] have shown that dust particles in the marine boundary layer remained hydrophobic even at high values of relative humidity, whereas this is low in the SAL, inhibiting particle growth.

Henceforth, these differences point to potential inhomogeneity in the vertical profile of dust during transport and indicate that the surface measurements may not be representative of the full atmospheric column. Analysis of CALIPSO/CALIOP observations, Liu *et al.* [2008] have shown that the marine boundary layer and the major dust plumes in the Saharan Air Layer (SAL) are decoupled at both ends of transport, close to the African coast where the dust-laden layers are at altitude and over the Caribbean when dust particles enter the MBL by regional-scale mixing.

influences [Novakov *et al.*, 1994, 1997; Mayol-Bracero *et al.*, 2001]. However, the occurrence and magnitude of peaks of particles in the submicron fraction (N_{sub}), during both dust and background periods, are associated with pollutants such as NO_2 and CO during daytime and with secondary O_3 during nighttime (Figure 5). Figure 10a illustrates the air mass arrival directions estimated from the local wind direction during dust events and their relation to N_{sub} , demonstrating that air masses characterized by N_{sub} exceeding 500 cm^{-3} are most frequently associated with southeastern winds, whereas N_{sub} lower than 500 cm^{-3} are mostly associated with easterly and northeasterly winds. South-east air masses are also associated with lower values of ω_0 in the PM_{10} fraction, that is, with more absorbing aerosols than in easterly air masses (Figure 10b). The low ω_0 in conjunction with the correlation with NO_2 and CO suggests that daytime submicron particles may be due to combustion processes. The concentrations of CO observed at CPR tend to be lower than previously found in Bermuda by Dickerson *et al.* [1995] both for local marine air masses and for air masses characteristic of long-range pollution transported from North America. By contrast, the observed values of NO_2 at CPR were significantly higher than the mixing ratios reported for marine (~ 20 ppt) and continental air (280 ppt) in Bermuda [Dickerson *et al.*, 1995].

As suggested by Allan *et al.* [2008], we attribute these peaks to transport of primary or nucleated but already grown particles in polluted air masses from the wider Caribbean island region, characterized by major ship track (<http://www.marinetraffic.com/>), rather than to local new particle formation. As a matter of fact, assuming that newly formed particles in the boundary layer have a growth rate in the range $1\text{--}20 \text{ nm h}^{-1}$ [Seinfeld and Pandis, 1997], the growth time corresponding to the modal diameter of the particles below 20 nm observed at the site should be of the order of 1 to 20 h. At the average wind speed of 6 m s^{-1} measured at the site, this corresponds to distances between 22 and 440 km, consistent with the minimum and maximum distances to the Caribbean islands south-east of CPR.

5. Conclusions

This study provides a description of African mineral dust transported across the Atlantic Ocean to the Caribbean. Several complementary techniques, including in situ measurements, remote sensing retrievals, and modeling analysis, have been used to characterize the mass concentration, size distribution, and optical properties of dust plumes after their transatlantic transport, and to link these properties with their source regions and transport pathways. Given the occurrence and the large spatial coverage of transatlantic dust transport, mineral dust can impact a wide range of environmental processes over a broad region that extends from the southern United States to the Amazon Basin. Dust particles sampled at Puerto Rico can likely be considered as representative of a relatively remote West Atlantic oceanic location.

Five dust events occurring from 21 June to 10 July 2012, each lasting 2–4 days and occurring regularly (every 1–2 days) were identified during the campaign. This transport strongly affected PM levels at Puerto Rico with PM_{10} concentrations increasing from 20 (regional background) to $70 \mu\text{g m}^{-3}$. The magnitude and persistence of mineral dust carried to the Caribbean suggest that dust is a prominent component in the region in the summer. The visual combination of satellite observations, numerical simulations, and backward trajectories gives strength to the source identification and duration of transatlantic transport: mineral dust originated from a wide range of sources in the Western Sahara/Mauritania, Algeria, Niger/Mali, and in the Bodelé Depression and reached Puerto Rico after 6–8 days of transport. Although almost localized source areas can be identified, the extent of those areas and the length of transport smooth out any regional feature at the receptor site.

The absorption properties of the dust plumes, represented by the mass absorption efficiency (MAE), were quite uniform among episodes. Some variability in the mass scattering efficiency (MSE) is attributed to changes in the relative proportions of the particle modes in the size distributions. When the air masses came from a southeasterly direction, the ω_0 in the PM_{10} fraction decreased from 0.97–0.98 to 0.92 at midvisible wavelengths. During such periods, high concentrations of fine particles (up to 6000 cm^{-3}) together with peaks of NO_2 concentration suggest a contamination of the dust plumes by marine traffic activities from the Caribbean Island region. The mixing in of ship traffic contaminated air did not affect the ω_0 of mineral dust in the PM_{10} fraction. We therefore recommend mass extinction efficiency (MEE) values in the range $1.1\text{--}1.5 \text{ m}^2 \text{ g}^{-1}$ and ω_0 values in the range 0.97–0.98 at midvisible wavelengths for long-range transported

dust across the Atlantic. These values are in the same range as observations made after short-range transport, suggesting that dust undergoes little modification during long-range transport over the Atlantic.

Dust plumes contained a significant fraction of large particles after undergoing more than 5000 km transport away from their source. The volume distributions during dust events peak at 2–3 μm in diameter and showed little variability in the modal position from one event to another. Comparison of column-average volume size distributions from AERONET with in situ ground-based measurements suggested some enhancement of the particle coarse fraction with altitude above the marine boundary layer. Comparison of size distributions obtained after long-range transport with size distributions at the dust emission source and near-source regions suggests that (1) the size distribution of transported dust is independent of the source region and (2) the modal diameter of coarse particles in dust plumes depends on height of transport and might remain relatively unchanged during transport across the Atlantic.

A first implication of our results is that they justify the common practice in models to treat dust size distributions as independent of source region. The fraction of coarse particles in the dust mass concentration decreases at short time (<1 day) after emission. The fraction of coarse dust particles remains largely unchanged despite the long-range transatlantic transport in summer, regardless of the spatial and temporal characteristics of the transport. The evolution of the dust size distribution as the plumes travel across the Atlantic is not exclusively controlled by dry deposition as a function of transport height. This could explain the difficulty models have in reproducing the transport of large dust particles [Mahowald *et al.*, 2014]. While the mechanism responsible for this phenomenon warrants further study, our observations suggest that a single parameterization of dust size distribution could be used in models over a wide range of spatial scales, from near sources to remote sites over the Atlantic.

This well-constrained new data set of dust optical and microphysical properties will be useful to the modeling community for validation exercises [Huneeus *et al.*, 2011]. Note that a larger than presented data set is available (including mass concentration) upon simple request for these purposes. The data set should also be taken into account for assessing the dust radiative effects in the shortwave and longwave and the impact of dust on ocean and forest productivity.

Acknowledgments

This project was funded by the Partner University Fund, a program of the French Embassy in the United States, and the FACE Foundation, with contributions from the National Science Foundation (NSF GEO AGS 0936879 grant), the Institute for Tropical Ecosystem Studies at the University of Puerto Rico-Rio Piedras, and the International Institute of Tropical Forestry USDA Forest Service, as part of the Luquillo Long-Term Ecological Research Program. We thank the Conservation Trust of Puerto Rico and their staff at the nature reserve of Cabezas de San Juan for allowing the use of their facilities to perform our study. The optical property data used in this paper are available from the WMO World Data Center for aerosols (<http://ebas.nilu.no/>). The remaining data are available from the DUST-MAP repository (<http://www.lisa.u-pec.fr/DustMAP/>).

References

- Allan, J. D., et al. (2008), Clouds and aerosols in Puerto Rico—A new evaluation, *Atmos. Chem. Phys.*, *8*, 1293–1309, doi:10.5194/acp-8-1293-2008.
- Allan, J. D., et al. (2015), G.: Iodine observed in new particle formation events in the Arctic atmosphere during ACCACIA, *Atmos. Chem. Phys.*, *15*, 5599–5609, doi:10.5194/acp-15-5599-2015.
- Anderson, T. L., and J. A. Ogren (1998), Determining aerosols radiative properties using the TSI 3563 integrating nephelometer, *Aerosol Sci. Technol.*, *29*, 57–69.
- Anderson, T. L., et al. (1996), Performance characteristics of a high-sensitivity, three-wavelength, total scatter/backscatter nephelometer, *J. Atmos. Oceanic Technol.*, *13*, 967–986.
- Ansmann, A., A. Petzold, K. Kandler, I. Tegen, M. Wendisch, D. Müller, B. Weinzierl, T. Müller, and J. Heintzenberg (2011), Saharan mineral dust experiments SAMUM-1 and SAMUM-2: What have we learned?, *Tellus, Ser. B*, *63*(4), 403–429.
- Bauer, S. E., Y. Balkanski, M. Schulz, D. A. Hauglustaine, and F. Dentener (2004), Global modeling of heterogeneous chemistry on mineral aerosol surfaces: Influence on tropospheric ozone chemistry and comparison to observations, *J. Geophys. Res.*, *109*, D02304, doi:10.1029/2003JD003868.
- Ben-Ami, Y., I. Koren, and O. Altaratz (2009), Patterns of North African dust transport over the Atlantic: Winter vs. summer, based on CALIPSO first year data, *Atmos. Chem. Phys.*, *9*(20), 7867–7875.
- Bohren, C. F., and D. R. Huffman (2007), *Absorption and Scattering of Light by Small Particles*, edited by C. F. Bohren and D. R. Huffman, pp. i–xiv, Wiley, New York.
- Bond, T. C., T. L. Anderson, and D. Campbell (1999), Calibration and intercomparison of filter-based measurements of visible light absorption by aerosols, *Aerosol Sci. Technol.*, *30*(6), 582–600.
- Boucher, O., et al. (2013), Clouds and aerosols, in *Climate Change 2013: The Physical Science Basis. Contribution of Working Group I to the Fifth Assessment Report of the Intergovernmental Panel on Climate Change*, edited by T. F. Stocker, et al., pp. 571–657, Cambridge Univ. Press, Cambridge, U. K., doi:10.1017/CBO9781107415324.016.
- Capes, G., J. G. Murphy, C. E. Reeves, J. B. McQuaid, J. F. Hamilton, J. R. Hopkins, J. Crosier, P. I. Williams, and H. Coe (2009), Secondary organic aerosol from biogenic VOCs over West Africa during AMMA, *Atmos. Chem. Phys.*, *9*, 3841–3850, doi:10.5194/acp-9-3841-2009.
- Chen, G., et al. (2011), Observations of Saharan dust microphysical and optical properties from the eastern Atlantic during NAMMA airborne field campaign, *Atmos. Chem. Phys.*, *11*(2), 723–740.
- Chiapello, I., and C. Moulin (2002), TOMS and Meteosat satellite records of the variability of Saharan dust transport over the Atlantic during the last two decades (1979–1997), *Geophys. Res. Lett.*, *29*(8), 1176, doi:10.1029/2001GL013767.
- Chiapello, I., C. Moulin, and J. M. Prospero (2005), Understanding the long-term variability of African dust transport across the Atlantic as recorded in both Barbados surface concentrations and large-scale total ozone mapping spectrometer (TOMS) optical thickness, *J. Geophys. Res.*, *110*, D18S10, doi:10.1029/2004JD005132.

- Chou, C., P. Formenti, M. Maille, P. Ausset, G. Helas, M. Harrison, and S. Osborne (2008), Size distribution, shape, and composition of mineral dust aerosols collected during the African monsoon multidisciplinary analysis special observation period 0: Dust and biomass-burning experiment field campaign in Niger, January 2006, *J. Geophys. Res.*, *113*, D00C10, doi:10.1029/2008JD009897.
- Colarco, P. R., E. P. Nowottnick, C. A. Randles, B. Yi, P. Yang, K.-M. Kim, J. A. Smith, and C. G. Bardeen (2014), Impact of radiatively interactive dust aerosols in the NASA GEOS-5 climate model: Sensitivity to dust particle shape and refractive index, *J. Geophys. Res. Atmos.*, *119*, 753–786, doi:10.1002/2013JD020046.
- Collins, D. R., et al. (2000), In situ aerosol size distributions and clear column radiative closure during ACE-2, *Tellus, Ser. B*, *52*, 498–525.
- Creamean, J. M., et al. (2013), Dust and biological aerosols from the Sahara and Asia influence precipitation in the western US, *Science*, *339*, 1572–1578, doi:10.1126/science.1227279.
- DeMott, P. J., K. Sassen, M. R. Poellot, D. Baumgardner, D. C. Rogers, S. D. Brooks, A. J. Prenni, and S. M. Kreidenweis (2003), African dust aerosols as atmospheric ice nuclei, *Geophys. Res. Lett.*, *30*(14), 1732, doi:10.1029/2003GL017410.
- Denjean, C., et al. (2016), Size distribution and optical properties of mineral dust aerosols transported in the western Mediterranean, *Atmos. Chem. Phys.*, *16*, 1081–1104, doi:10.5194/acp-16-1081-2016.
- de Reus, M., H. Fischer, R. Sander, V. Gros, R. Kormann, G. Salisbury, R. Van Dingenen, J. Williams, M. Zöllner, and J. Lelieveld (2005), Observations and model calculations of trace gas scavenging in a dense Saharan dust plume during MINATROC, *Atmos. Chem. Phys.*, *5*, 1787–1803, doi:10.5194/acp-5-1787-2005.
- Deroubaix, A., N. Martiny, I. Chiappello, and B. Marticorena (2013), Suitability of OMI aerosol index to reflect mineral dust surface conditions: Preliminary application for studying the link with meningitis epidemics in the Sahel, *Remote Sens. Environ.*, *133*, 116–127.
- Dickerson, R. R., B. G. Doddridge, P. Kelley, and K. P. Rhoads (1995), Large-scale pollution of the atmosphere over the remote Atlantic Ocean: Evidence from Bermuda, *J. Geophys. Res.*, *100*, 8945–8952, doi:10.1029/95JD00073.
- Dubovik, O., et al. (2006), Application of spheroid models to account for aerosol particle nonsphericity in remote sensing of desert dust, *J. Geophys. Res.*, *111*, D11208, doi:10.1029/2005JD006619.
- Duce, R. A., et al. (1991), The atmospheric input of trace species to the world ocean, *Global Biogeochem. Cycles*, *5*, 193–259, doi:10.1029/91GB01778.
- Dunion, J. P., and C. S. Velden (2004), The impact of the Saharan air layer on Atlantic tropical cyclone activity, *Bull. Am. Meteorol. Soc.*, *85*(3), 353–365.
- Dunkerton, T. J., M. T. Montgomery, and Z. Wang (2009), Tropical cyclogenesis in a tropical wave critical layer: Easterly waves, *Atmos. Chem. Phys.*, *9*, 5587–5646.
- Dupart, Y., et al. (2012), Mineral dust photochemistry induces nucleation events in the presence of SO₂, *Proc. Natl. Acad. Sci. U.S.A.*, *109*(51), 20,842–20,847.
- Engelstaedter, S., I. Tegen, and R. Washington (2006), North African dust emissions and transport, *Earth Sci. Rev.*, *79*, 73–100.
- Formenti, P., M. O. Andreae, L. Lange, G. Roberts, J. Cafmeyer, I. Rajta, W. Maenhaut, B. N. Holben, P. Artaxo, and J. Lelieveld (2001), Saharan dust in Brazil and Suriname during the Large-Scale Biosphere-Atmosphere Experiment in Amazonia (LBA)-Cooperative LBA Regional Experiment (CLAIRE) in March 1998, *J. Geophys. Res.*, *106*, 14,919–14,934, doi:10.1029/2000JD900827.
- Formenti, P., J. L. Rajot, K. Desboeufs, F. Saïd, N. Grand, S. Chevaillier, and C. Schmechtig (2011), Airborne observations of mineral dust over western Africa in the summer monsoon season: Spatial and vertical variability of physico-chemical and optical properties, *Atmos. Chem. Phys.*, *11*(13), 6387–6410.
- Formenti, P., S. Caquineau, K. Desboeufs, A. Klaver, S. Chevaillier, E. Journet, and J. L. Rajot (2014), Mapping the physico-chemical properties of mineral dust in western Africa: Mineralogical composition, *Atmos. Chem. Phys.*, *14*(19), 10,663–10,686.
- Garrett, T. J., L. M. Russell, V. Ramaswamy, S. F. Maria, and B. J. Huebert (2003), Microphysical and radiative evolution of aerosol plumes over the tropical North Atlantic Ocean, *J. Geophys. Res.*, *108*(D1), 4022, doi:10.1029/2002JD002228.
- Ginoux, P., and O. Torres (2003), Empirical TOMS index for dust aerosol: Applications to model validation and source characterization, *J. Geophys. Res.*, *108*(D17), 4534, doi:10.1029/2003JD003470.
- Ginoux, P., J. M. Prospero, T. E. Gill, C. Hsu, and M. Zhao (2012), Global scale attribution of anthropogenic and natural dust sources and their emission rates based on MODIS Deep Blue aerosol products, *Rev. Geophys.*, *50*, RG3005, doi:10.1029/2012RG000388.
- Haywood, J. M., P. Francis, S. Osborne, M. Glew, N. Loeb, E. Highwood, D. Tarré, G. Myhre, P. Formenti, and E. Hirst (2003), Radiative properties and direct radiative effect of Saharan dust measured by the C-130 aircraft during SHADE: 1. Solar spectrum, *J. Geophys. Res.*, *108*(D18), 8577, doi:10.1029/2002JD002687.
- Haywood, J. M., et al. (2008), Overview of the dust and biomass-burning experiment and African monsoon multidisciplinary analysis special observing period-0, *J. Geophys. Res.*, *113*, D00C17, doi:10.1029/2008JD010077.
- Haywood, J. M., et al. (2011), Motivation, rationale and key results from the GERBILS Saharan dust measurement campaign, *Q. J. R. Meteorol. Soc.*, *137*(658), 1106–1116.
- Heintzenberg, J. (2009), The SAMUM-1 experiment over Southern Morocco: Overview and introduction, *Tellus, Ser. B*, *61*(1), 2–11.
- Hinds, W. C. (1999), *Aerosol Technology: Properties, Behavior, and Measurement of Airborne Particles*, 504 pp., John Wiley, Chichester, U. K.
- Holben, B. N., et al. (2001), An emerging ground-based aerosol climatology: Aerosol optical depth from AERONET, *J. Geophys. Res.*, *106*, 12,067–12,097, doi:10.1029/2001JD900014.
- Huneus, N., M. Schulz, et al. (2011), Global dust model intercomparison in AeroCom phase I, *Atmos. Chem. Phys.*, *11*(15), 7781–7816.
- Jeong, M.-J., S.-C. Tsay, Q. Ji, N. C. Hsu, R. A. Hansell, and J. Lee (2008), Ground-based measurements of airborne Saharan dust in marine environment during the NAMMA field experiment, *Geophys. Res. Lett.*, *35*, L20805, doi:10.1029/2008GL035587.
- Jickells, T., and L. J. Spokes (2001), Atmospheric iron inputs to the oceans, in *The Biogeochemistry of Iron in Seawater, SCOR-IUPAC Ser.*, edited by D. R. Turner and K. A. Hunter, pp. 85–121, John Wiley, Baltimore, Md.
- Kandler, K., et al. (2009), Size distribution, mass concentration, chemical and mineralogical composition and derived optical parameters of the boundary layer aerosol at Tinfou, Morocco, during SAMUM 2006, *Tellus, Ser. B*, *61*, 32–50, doi:10.1111/j.1600-0889.2008.00385.x.
- Karyampudy, V. M., et al. (1999), Validation of the Saharan dust plume conceptual model using Lidar, Meteosat, and ECMWF data, *Bull. Am. Meteorol. Soc.*, *80*(6), 1045–1075.
- Kellogg, C. A., and D. W. Griffin (2006), Aerobiology and the global transport of desert dust, *Trends Ecol. Evol.*, *21*(11), 638–644.
- Kim, D., et al. (2014), Sources, sinks, and transatlantic transport of North African dust aerosol: A multimodel analysis and comparison with remote sensing data, *J. Geophys. Res. Atmos.*, *119*, 6259–6277, doi:10.1002/2013JD021099.
- Kwon, H., S. H. Cho, Y. Chun, F. Lagarde, and G. Pershagen (2002), Effects of the Asian dust events on daily mortality in Seoul, Korea, *Environ. Res.*, *90*, 1–5.
- Laurent, B., B. Marticorena, G. Bergametti, J. F. Léon, and N. M. Mahowald (2008), Modeling mineral dust emissions from the Sahara desert using new surface properties and soil database, *J. Geophys. Res.*, *113*, D14218, doi:10.1029/2007JD009484.

- Liu, Y., and P. Daum (2000), The effect of refractive index on size distributions and light scattering coefficients derived from optical particle counters, *J. Aerosol Sci.*, *31*(8), 945–957.
- Liu, Z., et al. (2008), CALIPSO lidar observations of the optical properties of Saharan dust: A case study of long-range transport, *J. Geophys. Res.*, *113*, D07207, doi:10.1029/2007JD008878.
- Mahowald, N., S. Albani, J. F. Kok, S. Engelstaeder, R. Scanza, D. S. Ward, and M. G. Flanner (2014), The size distribution of desert dust aerosols and its impact on the Earth system, *Aeolian Res.*, *15*, 53–71.
- Malmgren, B. A., and A. Winter (1999), Climate zonation in Puerto Rico based on principal components analysis and an artificial neural network, *J. Clim.*, *12*, 977–985.
- Maring, H., D. L. Savoie, M. A. Izaguirre, L. Custals, and J. S. Reid (2003a), Mineral dust aerosol size distribution change during atmospheric transport, *J. Geophys. Res.*, *108*(D19), 8592, doi:10.1029/2002JD002536.
- Maring, H., D. L. Savoie, M. A. Izaguirre, L. Custals, and J. S. Reid (2003b), Vertical distributions of dust and sea-salt aerosols over Puerto Rico during PRIDE measured from a light aircraft, *J. Geophys. Res.*, *108*(D19), 8587, doi:10.1029/2002JD002544.
- Martcorena, B., and G. Bergametti (1995), Modelling the atmospheric dust cycle: 1. Design of a soil derived dust production scheme, *J. Geophys. Res.*, *100*, 16,415–16,430, doi:10.1029/95JD00690.
- Martcorena, B., G. Bergametti, B. Aumont, Y. Callot, C. N'Doumé, and M. Legrand (1997), Modeling the atmospheric dust cycle: 2. Simulations of Saharan dust sources, *J. Geophys. Res.*, *102*, 4387–4404, doi:10.1029/96JD02964.
- Mayol-Bracero, O. L., O. Rosario, C. E. Corrigan, R. Morales, I. Torres, and V. Perez (2001), Chemical characterization of submicron organic aerosols in the tropical trade winds of the Caribbean using gas chromatography/mass spectrometry, *Atmos. Environ.*, *35*, 1735–1745.
- McConnell, C., E. J. Highwood, H. Coe, P. Formenti, B. Anderson, S. Osborne, S. Nava, K. Desboeufs, G. Chen, and M. A. J. Harrison (2008), Seasonal variations of the physical and optical characteristics of Saharan dust: Results from the Dust Outflow and Deposition to the Ocean (DODO) experiment, *J. Geophys. Res.*, *113*, D14S05, doi:10.1029/2007JD009606.
- McConnell, C. L., P. Formenti, E. J. Highwood, and M. A. J. Harrison (2010), Using aircraft measurements to determine the refractive index of Saharan dust during the DODO experiments, *Atmos. Chem. Phys.*, *10*(6), 3081–3098.
- Müller, K., S. Lehmann, D. van Pinxteren, T. Gnauk, N. Niedermeier, A. Wiedensohler, and H. Herrmann (2010), Particle characterization at the Cape Verde atmospheric observatory during the 2007 RHaMBLe intensive, *Atmos. Chem. Phys.*, *10*(6), 2709–2721.
- Ndour, M., B. D'Anna, C. George, O. Ka, Y. Balkanski, J. Kleffmann, K. Stemmler, and M. Ammann (2008), Photoenhanced uptake of NO₂ on mineral dust: Laboratory experiments and model simulations, *Geophys. Res. Lett.*, *35*, L05812, doi:10.1029/2007GL032006.
- Novakov, T., C. Riveracarpio, J. E. Penner, and C. F. Rogers (1994), The effect of anthropogenic sulfate aerosols on marine cloud droplet concentrations, *Tellus, Ser. B*, *46*, 132–141.
- Novakov, T., C. E. Corrigan, J. E. Penner, C. C. Chuang, O. Rosario, and O. L. Mayol-Bracero (1997), Organic aerosols in the Caribbean trade winds: A natural source? *J. Geophys. Res.*, *102*, 21,307–21,313, doi:10.1029/97JD01487.
- O'Dowd, C. D., and G. De Leeuw (2007), Marine aerosol production: A review of the current knowledge, *Philos. Trans. R. Soc. A*, *365*, 1753–1774.
- Ogren, J. A. (2010), Comment on “Calibration and intercomparison of filter-based measurements of visible light absorption by aerosols”, *Aerosol Sci. Technol.*, *44*(8), 589–591, doi:10.1080/02786826.2010.482111.
- Okada, K., J. Heintzenberg, K. Kai, and Y. Qin (2001), Shape of atmospheric mineral particles collected in three Chinese arid-regions, *Geophys. Res. Lett.*, *28*, 3123–3126, doi:10.1029/2000GL012798.
- Ortega, I. K., et al. (2012), New insights into nocturnal nucleation, *Atmos. Chem. Phys.*, *12*, 4297–4312.
- Osborne, S. R., B. T. Johnson, J. M. Haywood, A. J. Baran, M. A. J. Harrison, and C. L. McConnell (2008), Physical and optical properties of mineral dust aerosol during the dust and biomass-burning experiment, *J. Geophys. Res.*, *113*, D00C03, doi:10.1029/2007JD009551.
- Perez, L., A. Tobias, X. Querol, N. Künzli, J. Pey, A. Alastuev, M. Viana, N. Valero, M. González-Cabré, and J. Sunyer (2008), Coarse particles from Saharan dust and daily mortality, *Epidemiology*, *19*, 800–807.
- Petzold, A., et al. (2009), Saharan dust absorption and refractive index from aircraft-based observations during SAMUM 2006, *Tellus, Ser. B*, *61*(1), 118–130.
- Pico, R. (1974), *The Geography of Puerto Rico*, pp. 26–33, Aldine Co., Chicago, Ill.
- Prospero, J. M. (1999), Long-term measurements of the transport of African mineral dust to the southeastern United States: Implications for regional air quality, *J. Geophys. Res.*, *104*, 15,917–15,928, doi:10.1029/1999JD900072.
- Prospero, J. M., P. Ginoux, O. Torres, S. E. Nicholson, and T. E. Gill (2002), Environmental characterization of global sources of atmospheric soil dust identified with the Nimbus 7 total ozone mapping spectrometer (TOMS) absorbing aerosol product, *Rev. Geophys.*, *40*(1), 1002, doi:10.1029/2000RG000095.
- Raga, G. B., D. Baumgardner, and O. L. Mayol-Bracero (2016), History of aerosol-cloud interactions derived from observations in mountaintop clouds in Puerto Rico, *Aerosol Air Qual. Res.*, *16*(3), 674–688, doi:10.4209/aaqr.2015.05.0359.
- Redelsperger, J.-L., C. D. Thorncroft, A. Diedhiou, T. Lebel, D. J. Parker, and J. Polcher (2006), African monsoon multidisciplinary analysis: An international research project and field campaign, *Bull. Am. Meteorol. Soc.*, *87*(12), 1739–1746.
- Reid, J. S., and H. B. Maring (2003), Foreword to special section on the Puerto Rico Dust Experiment (PRIDE), *J. Geophys. Res.*, *108*(D19), 8585, doi:10.1029/2003JD0035102003.
- Reid, J. S., D. L. Westphal, J. M. Livingston, D. L. Savoie, H. B. Maring, H. H. Jonsson, D. P. Eleuterio, J. E. Kinney, and E. A. Reid (2002), Dust vertical distribution in the Caribbean during the Puerto Rico Dust Experiment, *Geophys. Res. Lett.*, *29*(7), 1151, doi:10.1029/2001GL014092.
- Reid, J. S., et al. (2003a), Comparison of size and morphological measurements of coarse mode dust particles from Africa, *J. Geophys. Res.*, *108*(D19), 8593, doi:10.1029/2002JD002485.
- Reid, J. S., et al. (2003b), Analysis of measurements of Saharan dust by airborne and ground-based remote sensing methods during the Puerto Rico Dust Experiment (PRIDE), *J. Geophys. Res.*, *108*(D19), 8586, doi:10.1029/2002JD002493.
- Reid, J. S., E. A. Reid, A. Walker, S. Piketh, S. Cliff, A. A. Mandoos, S.-C. Tsay, and T. F. Eck (2008), Dynamics of southwest Asian dust particle size characteristics with implications for global dust research, *J. Geophys. Res.*, *113*, D14212, doi:10.1029/2007JD009752.
- Ryder, C. L., et al. (2013a), Optical properties of Saharan dust aerosol and contribution from the coarse mode as measured during the Fennect 2011 aircraft campaign, *Atmos. Chem. Phys.*, *13*(1), 303–325.
- Ryder, C. L., E. J. Highwood, T. M. Lai, H. Sodemann, and J. H. Marsham (2013b), Impact of atmospheric transport on the evolution of microphysical and optical properties of Saharan dust, *Geophys. Res. Lett.*, *40*, 2433–2438, doi:10.1002/grl.50482.
- Schläditz, A., T. Müller, N. Kaaden, A. Massling, K. Kandler, M. Ebert, S. Weinbruch, C. Deutscher, and A. Wiedensohler (2009), In situ measurements of optical properties at Tinfou (Morocco) during the Saharan mineral dust experiment SAMUM 2006, *Tellus, Ser. B*, *61*(1), 64–78.
- Seinfeld, J. H., and S. N. Pandis (Eds) (1997), *Atmospheric Chemistry and Physics: From Air Pollution to Climate Change*, 1326 pp., John Wiley, New York.

- Sheridan, P. J., D. J. Delene, and J. A. Ogren (2001), Four years of continuous surface aerosol measurements from the Department of Energy's Atmospheric Radiation Measurement Program Southern Great Plains Cloud and Radiation Testbed site, *J. Geophys. Res.*, *106*, 20,735–20,747, doi:10.1029/2001JD000785.
- Spiegel, J., N. Buchmann, O. Mayol-Bracero, L. Cuadra-Rodriguez, C. Valle Díaz, K. Prather, S. Mertes, and W. Eugster (2014), Do cloud properties in a Puerto Rican tropical montane cloud forest depend on occurrence of long-range transported African dust?, *Pure Appl. Geophys.*, *171*(9), 2443–2459.
- Thorncroft, C., and K. Hodges (2001), African easterly wave variability and its relationship to Atlantic tropical cyclone activity, *J. Clim.*, *14*, 1166–1179.
- Todd, M. C., R. Washington, J. V. Martins, O. Dubovik, G. Lizcano, S. M'Bainayel, and S. Engelstaedter (2007), Mineral dust emission from the Bode'le' Depression, northern Chad, during BoDEx 2005, *J. Geophys. Res.*, *112*, D06207, doi:10.1029/2006JD007170.
- Torres, O., A. Tanskanen, B. Veihelmann, C. Ahn, R. Braak, P. K. Bhartia, P. Veefkind, and P. Levelt (2007), Aerosols and surface UV products from Ozone Monitoring Instrument observations: An overview, *J. Geophys. Res.*, *112*, D24S47, doi:10.1029/2007JD008809.
- Usher, C. R., A. Michel, and V. H. Grassian (2003), Reactions on mineral dust, *Chem. Rev.*, *103*, 4883–4940.
- Valle-Díaz, C. J., E. T. Torres-Delgado, S. M. Colón-Santos, T. Lee, J. L. Collett Jr., W. H. McDowell, and O. L. Mayol-Bracero (2016), Impact of long-range transported African dust on cloud water chemistry at a tropical montane cloud forest in northeastern Puerto Rico, *Aerosol Air Qual. Res.*, *16*(3), 653–664, doi:10.4209/aaqr.2015.05.0320.
- van den Heever, S. C., G. G. Carrié, W. R. Cotton, P. J. DeMott, and A. J. Prenni (2006), Impacts of nucleating aerosol on Florida storms. Part I: Mesoscale simulations, *J. Atmos. Sci.*, *63*, 1752–1775, doi:10.1175/JAS3713.1.
- Washington, R., M. Todd, N. J. Middleton, and A. S. Goudie (2003), Dust-storm source areas determined by the total ozone monitoring spectrometer and surface observations, *Ann. Assoc. Am. Geogr.*, *93*, 297–313.
- Washington, R., et al. (2012), Fennec—The Saharan climate system, *CLIVAR Exch.*, *17*(3), 31–32.
- Weinzierl, B., A. Petzold, M. Esselborn, M. Wirth, K. Rasp, K. Kandler, L. Schütz, P. Koepke, and M. Fiebig (2009), Airborne measurements of dust layer properties, particle size distribution and mixing state of Saharan dust during SAMUM 2006, *Tellus, Ser. B*, *61*(1), 96–117.
- Weinzierl, B., et al. (2011), Microphysical and optical properties of dust and tropical biomass burning aerosol layers in the Cape Verde region—An overview of the airborne in situ and lidar measurements during SAMUM-2, *Tellus, Ser. B*, *63*(4), 589–618.
- Yue, X., H. Liao, H. J. Wang, S. L. Li, and J. P. Tang (2011), Role of sea surface temperature responses in simulation of the climatic effect of mineral dust aerosol, *Atmos. Chem. Phys.*, *11*(12), 6049–6062.